FIELD-BASED PHASE RETRIEVAL USING UNDER-SAMPLED DATA

THESIS

Tatsuki L. Watts, 2nd Lieutenant, USAF

AFIT-ENG-MS-16-M-051

DEPARTMENT OF THE AIR FORCE
AIR UNIVERSITY

AIR FORCE INSTITUTE OF TECHNOLOGY

Wright-Patterson Air Force Base, Ohio

AFIT-ENG-MS-16-M-051

FIELD-BASED PHASE RETRIEVAL USING UNDER-SAMPLED DATA

THESIS

Presented to the Faculty

Department of Electrical and Computer Engineering

Graduate School of Engineering and Management

Air Force Institute of Technology

Air University

Air Education and Training Command

In Partial Fulfillment of the Requirements for the

Degree of Master of Science in Electrical Engineering

Tatsuki L. Watts, BS

2nd Lieutenant, USAF

March 2016

AFIT-ENG-MS-16-M-051

FIELD-BASED PHASE RETRIEVAL USING UNDER-SAMPLED DATA

Tatsuki L. Watts, BS
2nd Lieutenant, USAF

Committee Membership:

Stephen C. Cain, PhD
Chair

Capt Kevin P. Vitayaudom
Member

Benjamin F. Akers, PhD
Member

AFIT-ENG-MS-16-M-051

Abstract

A phase retrieval algorithm designed for use with under-sampled astronomical data is developed in this thesis. Blind-deconvolution, Gerchberg Saxton (GS), and a field-based compass search are combined into an algorithm capable of recovering Zernike coefficients 4 through 11 from single frames of noisy, under-sampled data without the need to unwrap the recovered phase. The performance of the algorithm in data under-sampled by a factor of 2 is compared the performance of the algorithm on Nyquist-sampled data.

In simulation trials, the magnitudes of all 8 estimated Zernike coefficients converged to within half a wave of the true values for 98% of the Nyquist-sampled frames and 92% under-sampled frames. The simulation was conducted using 100 frames of point-source data generated by randomly choosing Zernike coefficients 2 through 11 from a normal distribution. In addition to the simulation, phase retrieval was performed on defocused data and data containing an astigmatism aberration. For the astigmatism data, the estimated Zernike coefficient magnitudes were within $1/10^{th}$ of a wave for Nyquist data and $1/5^{th}$ of a wave for data under-sampled by a factor of 2. The magnitude of defocus recovered from Nyquist-sampled data was within 0.02 waves of the value predicted using defocus recovered from data under-sampled by 2.

Acknowledgments

I would like to express my sincere appreciation to my faculty advisor, Dr. Stephen Cain, for his guidance and support throughout the course of this thesis effort. The insight and experience was certainly appreciated.

Tatsuki L. Watts

Table of Contents

Page

List of Figures

List of Tables

Table Page

List of Symbols

FIELD-BASED PHASE RETRIEVAL USING UNDER-SAMPLED DATA

I. Introduction

Importance of Space Situational Awareness

One facet of Space Domain Awareness (SDA) is the ability to track satellites and debris in orbit around the Earth. Two events highlighted the importance of SDA in the late 2000's. The first event occurred in 2007 when China shot down one of its own satellites with a developmental anti-satellite missile (ASAT) [1]. The second event occurred in 2009 when Iridium 33 collided with Cosmos 2251, a defunct Russian satellite [2]. Both events created thousands of pieces of debris, which continue to threaten satellites and spacecraft today. Even small pieces of debris can cause significant damage due to the high velocities at which they travel. It is theorized that the amount of space debris will grow exponentially over time as existing debris collides with other objects to create more objects.

The vulnerability of space assets coupled with the US military's operational reliance on these assets has made SDA a priority for national defense. The 2015 National Security Strategy states: "We will also develop technologies and tactics to deter and defeat efforts to attack our space systems; enable indications, warning, and attributions of such attacks; and enhance the resiliency of critical U.S. space capabilities" [3]. Developing technologies that facilitate the population of the space catalog is the primary focus of this research.

Motivation

The Joint Space Operations Center (JSpOC) maintains SDA for the U.S. government using RADAR and optical systems. The focus of this thesis is on ground-based telescopes such as the Ground Based Electro-Optical Deep Space Surveillance Telescope and its successor, the Space Surveillance Telescope.

In 2011, the National Research Council (NRC) conducted a study on the effectiveness of the algorithms used by the JSpOC to detect and track objects in orbit. A key system limitation identified by the NRC was the "…understanding of the quality of the observations, and the challenge of fusing disparate data from different systems and phenomenology." The goal of this thesis is to develop the ability to regularly quantify optical aberrations, which could serve as a useful measure of observation quality for optical telescopes.

Background

Phase retrieval algorithms determine the effective aperture phase from the impulse response, or point-spread function (PSF), of the optical system. General phase retrieval algorithms have been investigated by Feinup, his most notable accomplishment being the characterization of the Hubble Space Telescope [4]. However, Feinup's work sought to estimate the entire aperture plane phase, instead of constraining phase retrieval to an estimation of low-order Zernike coefficients.

Algorithms with the ability to estimate Zernike coefficients from astronomical images exist. One such method is called the donut algorithm and is currently used to measure the aberrations of the Space Surveillance Telescope [5]. However, the donut algorithm

requires large amounts of defocus to be introduced into the image in order to be effective [6], which incurs operational downtime thereby preventing practical routine use of the algorithm. Another technique for estimating aberration coefficients involves the use of the Gerchberg-Saxton (GS) phase retrieval algorithm [7] together with phase unwrapping. Although the GS algorithm has been shown to recover useful estimates of optical phase errors, these estimates are only correct modulo 2π. Two-dimensional phase unwrapping is necessary to reproduce the original phase, from which Zernike coefficients may be recovered. Many phase-unwrapping algorithms exist, but none have been recognized as the definitive solution [8].

A technique capable of directly recovering aberrations from in-focus images without the need for phase unwrapping was developed at AFIT by Maj. Zingarelli [9]. Such an algorithm could be used to routinely characterize telescopes with no operational overhead. However, testing was performed under ideal conditions with Nyquist-sampled data.

Problem Statement

The goal of this research is to develop a new method based on Zingarelli's work that recovers optical phase aberrations from astronomical imagery that is under-sampled by a factor of two.

Thesis Outline

Chapter II introduces methods used to model telescopes and predict aberrations in terms of Zernike coefficients. Under-sampled blind deconvolution and the convergence of variance termination condition is discussed in Chapter III. The phase retrieval algorithm

is synthesized in Chapter IV and its performance is evaluated in Chapter V. Finally, Chapter VI concludes the thesis by describing the significance of the results and outlining areas for possible future research.

II. Optical Modeling

Background

Optical systems can be viewed as functions mapping objects to images, as shown in Figure 1 [10].

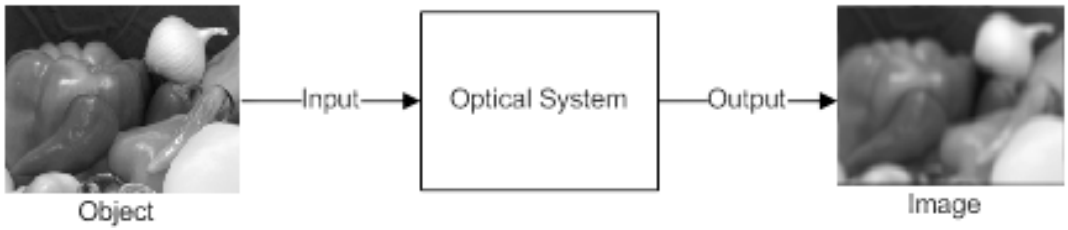

Figure 1: Optical system as a function.

An optical system's impulse response, or point-spread function (PSF), shown in Figure 2 describes how a single point of light is spread out by the imaging system [10]. The mapping in Figure 1 is often reduced to a two-dimensional convolution between the object and PSF by assuming the PSF remains constant over the image.

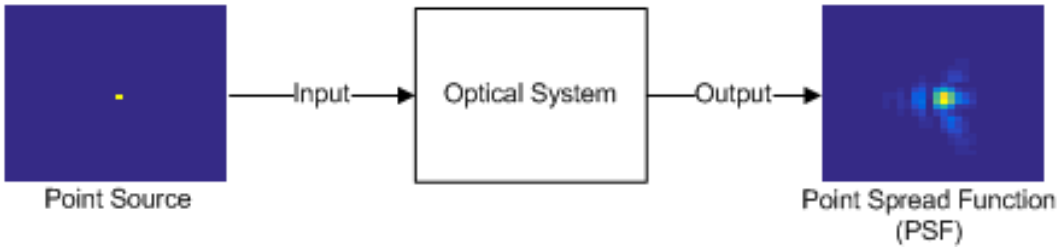

Figure 2: Point spread function (PSF).

Equation (2.1) shows the relationship between the PSF, $g(u,v)$, the aperture, $A(\eta,\xi)$, and the phase function, $\phi(\xi,\eta)$.

$$g(u,v)=\left|\iint A(\xi,\eta)e^{j\phi(\xi,\eta)}e^{-j\frac{2\pi}{\lambda z}(u\xi+v\eta)}d\xi d\eta\right|^2 \tag{2.1}$$

The aperture as well as the detector are approximated as being infinitely thin and thus contained within two-dimensional planes perpendicular to the optical axis, spanned by the coordinates (ξ,η) and (u,v), respectively. Additionally, the PSF is often normalized to sum to one as shown in (2.2), where $h(u,v)$ is the normalized PSF.

$$h(u,v)=\frac{g(u,v)}{\iint g(u,v)\,dudv} \tag{2.2}$$

In general, smaller PSFs are desirable because they produce images that better represent the object. Problematically, fluctuations in the phase function tend to increase the size of the PSF. These fluctuations can be reduced by physically improving the imaging system. However, the phase function itself is not directly measurable and must be estimated through phase retrieval techniques. Additionally, once the phase function is recovered, it must be decomposed into classical aberrations which convey physical meaning in terms of the optical configuration.

Luckily, the second issue was solved by Fritz Zernike, who invented a radially orthogonal set of functions known as the Zernike polynomials, where many correspond to classical aberrations. The strength of these aberrations are communicated by the size of the Zernike coefficients, α_i, associated with each polynomial. The bottom two rows of Figure 3 shows the degradation in image quality due to the presence of defocus and oblique astigmatism, which are classical aberrations corresponding to the 4th and 5th Zernike polynomials. The top row of Figure 3 shows the image obtained by and imaging system free of aberrations. Such an imaging system is said to be diffraction-limited since its performance is only limited by diffraction caused by the finite extent of its aperture.

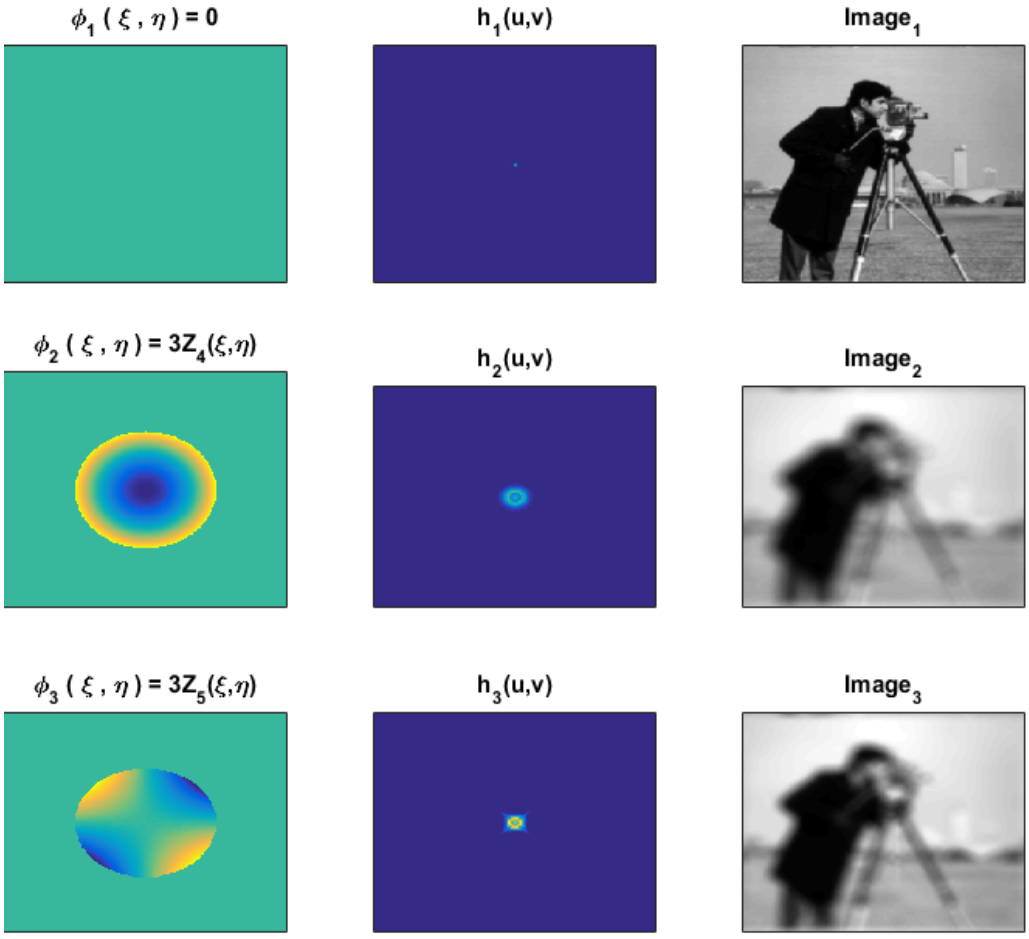

Figure 3: PSF effects on image.

Since the Zernike polynomials are radially orthogonal, these coefficients can be calculated by normalizing the inner product between the phase function and the i^{th} Zernike polynomial, $Z_i(\xi,\eta)$, as shown in (2.3), assuming a circular aperture.

$$\alpha_i = \frac{\iint \phi(\xi,\eta) Z_i(\xi,\eta) d\xi d\eta}{\iint Z_i(\xi,\eta)^2 d\xi d\eta} \tag{2.3}$$

Numerically, (2.3) is evaluated as shown in, where the aperture plane coordinates are discretized. Spatial sampling periods in the ξ and η direction are denoted by Δ_ξ and Δ_η, respectively and $(p,q) \in I$.

$$\alpha_i = \frac{\sum_{p,q} \phi(\Delta_\xi p, \Delta_\eta q) Z_i(\Delta_\xi p, \Delta_\eta q)}{\sum_{p,q} Z_i(\Delta_\xi p, \Delta_\eta q)^2} \tag{2.4}$$

The phase function is reconstructed from Zernike coefficients as shown in (2.5). Note that, in general, the reconstructed phase will only be an approximation unless infinite Zernike coefficients are used.

$$\phi(\xi,\eta) \approx \sum_i \alpha_i Z_i(\xi,\eta) \tag{2.5}$$

In our characterization of optical aberrations, we restrict our attention to the 11th Zernike polynomial and below in a similar manner to recent literature attempting to focus and align the Space Surveillance Telescope [5]. The first Zernike polynomial is also ignored because the corresponding aberration, piston, has no effect on the PSF, as shown in (2.6).

$$\begin{aligned} &\left| \iint A(\xi,\eta) e^{j\sum_{i=1}^{11} \alpha_i Z_i(\xi,\eta)} e^{-j\frac{2\pi}{\lambda z}(u\xi+v\eta)} d\xi d\eta \right|^2 \\ &= \left| e^{j\alpha_1} \iint A(\xi,\eta) e^{j\sum_{i=2}^{11} \alpha_i Z_i(\xi,\eta)} e^{-j\frac{2\pi}{\lambda z}(u\xi+v\eta)} d\xi d\eta \right|^2 \\ &= \left| \iint A(\xi,\eta) e^{j\sum_{i=2}^{11} \alpha_i Z_i(\xi,\eta)} e^{-j\frac{2\pi}{\lambda z}(u\xi+v\eta)} d\xi d\eta \right|^2 \end{aligned} \tag{2.6}$$

Predicting Zernike Coefficients

Under certain conditions, Zernike coefficients can be predicted to an extent limited by our knowledge of the optical configuration of the imaging system. To estimate Zernike coefficients, the phase function $\phi(\xi,\eta)$ is calculated as shown in in (2.7) and decomposed into Zernike coefficients using (2.3).

$$\phi(\xi,\eta) = k\left(r_{21}(x,y,\xi,\eta) + r_{01}(u,v,\xi,\eta) + t(\xi,\eta)\right) \tag{2.7}$$

In (2.7), the term $r_{21}(x,y,\xi,\eta)$ represents the distance from a point source to an arbitrary point within the aperture, whereas the term $r_{01}(u,v,\xi,\eta)$ represents the distance from an arbitrary point within the aperture to an arbitrary point on the detector. Like the aperture and detector, the object, in this case a point source, is also assumed to lie in a plane perpendicular to the optical axis spanned by coordinates (x,y). The term $t(\xi,\eta)$ represents the phase transformation induced by the optical elements of the imaging system and k is the wave number defined as shown in (2.8)

$$k = \frac{2\pi}{\lambda} \tag{2.8}$$

A simple optical setup where the phase function can be modeled using (2.7) is shown in Figure 4.

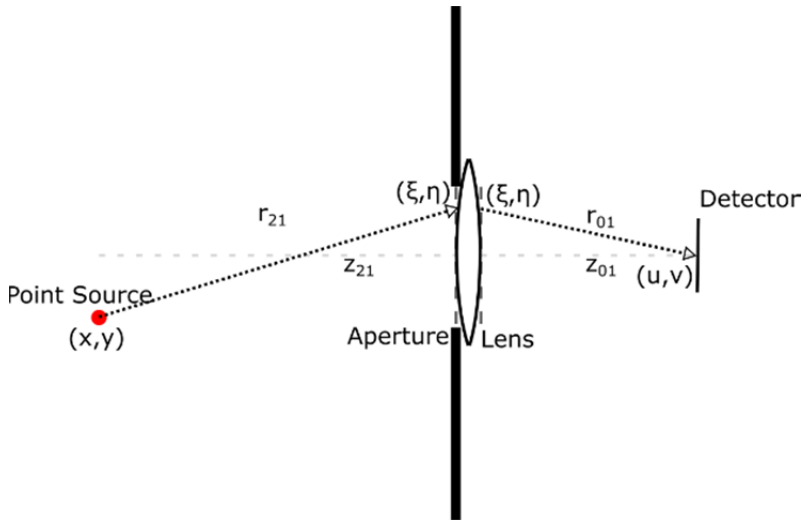

Figure 4: Optical setup.

The remainder of this section is dedicated deriving the conditions under which calculating the phase function as shown in (2.7) is mathematically valid. The Rayleigh-Sommerfeld diffraction equation (2.9), relates the field incident on the aperture plane, $U_A(\xi,\eta)$, to the field incident on the detector plane, $U_D(u,v)$, which are perpendicularly separated by distance z_{01}.

$$U_D(u,v) = \frac{z_{01}}{j\lambda}\iint U_A(\xi,\eta)\frac{e^{jkr_{01}(u,v,\xi,\eta)}}{r_{01}^2(u,v,\xi,\eta)}d\xi d\eta \tag{2.9}$$

The goal is to approximate the Rayleigh-Sommerfeld formula as the Fourier transform shown in (2.10), since the detector field is calculated from Zernike coefficients using the Fourier propagation shown in (2.11).

$$U_D(u,v) \approx \iint A(\xi,\eta)e^{jk(r_{21}(x,y,\xi,\eta)+r_{01}(u,v,\xi,\eta)+t(\xi,\eta))}e^{-j\frac{2\pi}{\lambda z_{01}}(u\xi+v\eta)}d\xi d\eta \tag{2.10}$$

$$U_D(u,v) = \iint A(\xi,\eta)e^{j\sum_i \alpha_i Z_i(\xi,\eta)}e^{-j\frac{2\pi}{\lambda z_{01}}(u\xi+v\eta)}d\xi d\eta \tag{2.11}$$

Only the argument of the leftmost complex exponentials differ between (2.10) and (2.11). For detector field produced by (2.10) and (2.11) to be consistent, (2.12) must be true.

$$\phi(\xi,\eta)=\sum_i \alpha_i Z_i(\xi,\eta)=k\left(r_{21}(x,y,\xi,\eta)+r_{01}(u,v,\xi,\eta)+t(\xi,\eta)\right) \tag{2.12}$$

First, an expression for the aperture field is substituted into the Rayleigh-Sommerfeld equation. To simulate an impulse response, the aperture field is set equal to the product of the spherically diverging field from a point source and the phase transformations induced by the optics, as shown in (2.13).

$$U_A(\xi,\eta)=A(\xi,\eta)\frac{e^{jk\left(r_{21}(x,y,\xi,\eta)+t(\xi,\eta)\right)}}{r_{21}(x,y,\xi,\eta)} \tag{2.13}$$

Substituting (2.13) into (2.9) gives (2.14).

$$U_D(u,v)=\frac{z_{01}}{j\lambda}\iint A(\xi,\eta)\frac{e^{jk\left(r_{21}(x,y,\xi,\eta)+r_{01}(u,v,\xi,\eta)+t(\xi,\eta)\right)}}{r_{21}(x,y,\xi,\eta)\,r_{01}^2(u,v,\xi,\eta)}d\xi d\eta \tag{2.14}$$

Assuming $z_{01}^2=(\xi-x)^2+(\eta-y)^2$ and $z_{21}^2=(\xi-u)^2+(\eta-v)^2$, where z_{21} is the perpendicular distance between the aperture plane and object plane, the substitutions shown in (2.15) are made in the denominator of (2.14), yielding (2.16). These substitutions only have a weak effect on the amplitude of the result and are universally accepted since they are used in the derivation of the Fresnel diffraction equation [10].

$$\begin{aligned} r_{21}(x,y,\xi,\eta)&=\sqrt{z_{21}^2+(\xi-x)^2+(\eta-y)^2}\approx z_{21}\\ r_{01}(\mathrm{u},\mathrm{v},\xi,\eta)&=\sqrt{z_{01}^2+(\xi-u)^2+(\eta-v)^2}\approx z_{01}\end{aligned} \tag{2.15}$$

$$U_D(u,v)=\frac{1}{j\lambda z_{21}z_{01}}\iint A(\xi,\eta)\,\mathrm{e}^{jk\left(r_{21}(x,y,\xi,\eta)+r_{01}(\mathrm{u},\mathrm{v},\xi,\eta)+t(\xi,\eta)\right)}\,d\xi d\eta \tag{2.16}$$

Traditionally, the Rayleigh-Sommerfeld equation must be evaluated separately for every point of interest in the detector plane. However, we are attempting to approximate the Rayleigh-Sommerfeld equation using a Fourier transform only evaluated once for the entire detector plane. Therefore, the Rayleigh-Sommerfeld formula is modified to calculate the detector field over an arbitrary region surrounding the point of interest by substituting $(u+u',v+v')$ for (u,v) as shown in (2.17), where u',v' are shifts from the point of interest.

$$U_D(u+u',v+v') = \frac{1}{j\lambda z_{21} z_{01}} \iint A(\xi,\eta)\, \mathrm{e}^{jk\left(r_{21}(x,y,\xi,\eta)+r_{01}(u+u',v+v',\xi,\eta)+t(\xi,\eta)\right)} d\xi d\eta \qquad (2.17)$$

The term $r_{01}(u+u',v+v',\xi,\eta)$ then, represents the distance to $(u+u',v+v')$, calculated as shown in (2.18).

$$r_{01}(u+u',v+v',\xi,\eta) = \sqrt{z_{01}^2 + \left(\xi-\left(u+u'\right)\right)^2 + \left(\eta-\left(v+v'\right)\right)^2} \qquad (2.18)$$

Regrouping terms in (2.18) gives (2.19) .

$$r_{01}(u+u',v+v',\xi,\eta) = \sqrt{z_{01}^2 + \left(\left(\xi-u\right)-u'\right)^2 + \left(\left(\eta-v\right)-v'\right)^2} \qquad (2.19)$$

$$\begin{aligned} \xi' &= \xi - u \\ \eta' &= \eta - v \end{aligned} \qquad (2.20)$$

$$r_{01}(u+u',v+v',\xi,\eta) = \sqrt{z_{01}^2 + \left(\xi'-u'\right)^2 + \left(\eta'-v'\right)^2} \qquad (2.21)$$

Performing the squares within the radical and regrouping results in (2.22).

$$r_{01}(u+u',v+v',\xi,\eta) = \sqrt{\left[z_{01}^2 + \xi'^2 + \eta'^2\right] - 2\xi'u' + u'^2 - 2\eta'v' + v'^2} \qquad (2.22)$$

Notice that the bracketed terms correspond to $r_{01}(u,v,\xi,\eta)$ from (2.15). Therefore, substitute (2.23) into (2.22) to get (2.24)

$$r_{01}^2(u,v,\xi,\eta) = z_{01}^2 + \left(\xi - u\right)^2 + \left(\eta - v\right)^2 = z_{01}^2 + \xi'^2 + \eta'^2 \tag{2.23}$$

$$r_{01}(u+u',v+v',\xi,\eta) = \sqrt{r_{01}^2(u,v,\xi,\eta) - 2\xi'u' + u'^2 + -2\eta'v' + v'^2} \tag{2.24}$$

Pulling $r_{01}(u,v,\xi,\eta)$ outside of the radical results in (2.25).

$$r_{01}(u+u',v+v',\xi,\eta) = r_{01}(u,v,\xi,\eta)\sqrt{1 + \frac{-2\xi'u' + u'^2 + -2\eta'v' + v'^2}{r_{01}^2(u,v,\xi,\eta)}} \tag{2.25}$$

The radical in (2.25) is replaced with its binomial approximation, consisting of the first two terms of its Taylor series. The Taylor series expansion of $\sqrt{1+b}$ is shown in (2.26).

$$\sqrt{1+b} = 1 + \frac{b}{2} - \frac{b^2}{8} + \frac{b^3}{16} - \frac{5b^4}{128}... \tag{2.26}$$

$$r_{01}(u+u',v+v',\xi,\eta) \approx r_{01}(u,v,\xi,\eta) + \frac{-2\xi'u' + u'^2 + -2\eta'v' + v'^2}{r_{01}(u,v,\xi,\eta)} \tag{2.27}$$

Note that the rightmost term within the radical in (2.25) corresponds to b in (2.26), as shown in (2.28).

$$b = \frac{-2\xi'u' + u'^2 + -2\eta'v' + v'^2}{r_{01}^2(u,v,\xi,\eta)} \tag{2.28}$$

The resulting equation, (2.27), is only valid when the product of the wave number and the sum of the third term onwards of the Taylor series expansion of (2.25) is much less than one.

$$e^{jk\sum -\frac{b^2}{8} + \frac{b^3}{16} - \frac{5b^4}{128}...} \approx e^0 = 1 \tag{2.29}$$

Since successive terms have alternating signs as well as diminishing magnitudes when $b < 1$, the third term of the series can be used as an upper bound for the sum of the terms neglected by the binomial approximation.

$$\left|-\frac{b^2}{8}\right| > \left|-\frac{b^2}{8}+\frac{b^3}{16}-\frac{5b^4}{128}\ldots\right| \tag{2.30}$$

Therefore, (2.27) is valid if the product of the wavenumber and the third term of the Taylor series expansion of (2.25) is much less than 1, as shown in (2.31).

$$\frac{kb^2}{8} = \frac{2\pi}{\lambda} r_{01}(u,v,\xi,\eta) \frac{\left(\frac{-2\xi'u' + u'^2 + -2\eta'v' + v'^2}{r_{01}^2(u,v,\xi,\eta)}\right)^2}{8} << 1 \tag{2.31}$$

Simplifying (2.31) gives (2.32).

$$\frac{\pi}{\lambda} \frac{\left(-2\xi'u' + u'^2 + -2\eta'v' + v'^2\right)^2}{4r_{01}^3(u,v,\xi,\eta)} << 1 \tag{2.32}$$

Since $r_{01} \geq z_{01}$, z_{01} is substituted for r_{01} to yield a simplified upper bound, as shown in (2.33).

$$\frac{\pi}{\lambda} \frac{\left(-2\xi'u' + u'^2 - 2\eta'v' + v'^2\right)^2}{4r_{01}^3(u,v,\xi,\eta)} \leq \frac{\pi}{\lambda} \frac{\left(-2\xi'u' + u'^2 - 2\eta'v' + v'^2\right)^2}{4z_{01}^3} \tag{2.33}$$

In (2.34), the triangle inequality is used to further simplify the upper bound.

$$\frac{\pi}{\lambda} \frac{\left(-2\xi'u' + u'^2 + -2\eta'v' + v'^2\right)^2}{4z_{01}^3} \leq \frac{\pi}{\lambda} \frac{\left(\left(u'^2 + v'^2\right) + 2\left(\left|\xi'\right|\left|u'\right| + \left|\eta'\right|\left|v'\right|\right)\right)^2}{4z_{01}^3} \tag{2.34}$$

Expanding the outermost square on the RHS of (2.34) produces three terms, the first of which is shown in (2.35).

$$\frac{\pi}{\lambda} \frac{\left(u'^2 + v'^2\right)^2}{4z_{01}^3} \tag{2.35}$$

It is useful to transform the spatial coordinates (u', v') into pixel coordinates (n, m) using the relationship in (2.36) predicted by the Nyquist-sampling theorem. The diffraction

limited maximum spatial frequency in the detector plane, given a circular pupil function is $\frac{D}{\lambda z_{01}}$, leading to a spatial sampling period of $\frac{\lambda z_{01}}{2D}$.

$$\begin{aligned} u' &= \frac{\lambda z_{01}}{2D} n \\ v' &= \frac{\lambda z_{01}}{2D} m \end{aligned} \tag{2.36}$$

Substituting (2.36) into (2.35) gives (2.37).

$$\frac{\pi}{\lambda} \frac{\left(\frac{\lambda z_{01}}{2D}\right)^4 \left(n^2 + m^2\right)^2}{4 z_{01}^3} = \frac{\pi \lambda^3 z_{01} \left(n^2 + m^2\right)^2}{64 D^4} \tag{2.37}$$

The expression in (2.37) can be simplified using the upper bound generated by substituting $n_{\max}$, defined in (2.38), for both n, m. The simplified expression is shown in (2.39).

$$n_{\max} = \max\{n, m\} \tag{2.38}$$

$$\frac{\pi \lambda^3 z_{01} n_{\max}^4}{64 D^4} \tag{2.39}$$

The second term yielded by the expansion of (2.34) is shown in (2.40).

$$\frac{\pi}{\lambda} \frac{\left(u'^2 + v'^2\right)\left(|\xi'||u'| + |\eta'||v'|\right)}{z_{01}^3} \tag{2.40}$$

The maximum values for both ξ' and η' are equal to half the aperture diameter plus the magnitude of the coordinate of the point of interest in the detector plane along the same dimension. However, since sensors are much smaller than the aperture diameter for telescopes, the maximum values for ξ' and η' are approximated as show in (2.41).

$$\max\{\xi'\} = \frac{D}{2} + |u| \approx \frac{D}{2}$$
$$\max\{\eta'\} = \frac{D}{2} + |v| \approx \frac{D}{2} \tag{2.41}$$

Substituting $\frac{D}{2}$ for ξ' and η' in (2.40) and transforming u' and v' to pixel coordinates using (2.36), gives the upper bound in (2.42).

$$\frac{\pi\left(u'^2 + v'^2\right)\left(|\xi'||u'| + |\eta'||v'|\right)}{\lambda z_{01}^3} \leq \frac{\left(\frac{\lambda z_{01}}{2D}\right)^3 \left(n^2 + m^2\right)\left(\left(\frac{D}{2}\right)\left(|n| + |m|\right)\right)}{\lambda z_{01}^3} \tag{2.42}$$

The upper bound is further simplified in (2.43) by substituting $n_{\max}$ for n and m.

$$\frac{\pi\lambda^2\left(n^2 + m^2\right)\left(\left(\frac{D}{2}\right)\left(|n| + |m|\right)\right)}{8D^3} \leq \frac{\pi\lambda^2 {n_{\max}}^3}{4D^2} \tag{2.43}$$

The third and final term from expanding (2.34) is shown in (2.44).

$$\frac{\pi}{\lambda}\frac{4\left(|\xi'||u'| + |\eta'||v'|\right)^2}{4z_{01}^3} \tag{2.44}$$

In a similar manner to the second term, the third term is simplified using an upper bound as shown in (2.45), where $\frac{D}{2} - u_{\max}$ is substituted for ξ', η' and spatial coordinates u', v' are transformed to pixel coordinates using (2.36).

$$\frac{\pi\left(|\xi'||u'| + |\eta'||v'|\right)^2}{\lambda z_{01}^3} \leq \frac{\pi\left(\frac{\lambda z_{01}}{2D}\right)^2 \left(\left(\frac{D}{2}\right)\left(|n| + |m|\right)\right)^2}{\lambda z_{01}^3} \tag{2.45}$$

In (2.46), the upper bound is further simplified by substituting $n_{\max}$ for n and m.

$$\frac{\pi\lambda\left(\left(\frac{D}{2}\right)\left(|n|+|m|\right)\right)^2}{2D^2 z_{01}} \leq \frac{\pi\lambda {n_{\max}}^2}{2z_{01}} \tag{2.46}$$

Therefore, the binomial approximation in (2.27) holds given (2.47) is satisfied.

$$\frac{\pi\lambda^3 z_{01} n_{\max}^4}{64D^4} + \frac{\pi\lambda^2 {n_{\max}}^3}{4D^2} + \frac{\pi\lambda {n_{\max}}^2}{2z_{01}} << 1 \tag{2.47}$$

Generally, wavelength is by far the smallest term. Therefore, (2.47) is practically satisfied if its rightmost term is much less than 1, as shown in (2.48).

$$\frac{\pi\lambda {n_{\max}}^2}{2z_{01}} << 1 \tag{2.48}$$

Note that (2.48) can be satisfied, even for large, short focal length telescopes such as the SST. Consider the impact of (2.48) on the maximum region size in the detector plane over which the field can be computed in terms of Nyquist-sampled pixels in (2.49).

$$n_{\max} << \sqrt{\frac{2z_{01}}{\pi\lambda}} = \sqrt{\frac{2(3.5m)}{\pi(.5\mu m)}} = 2111 \text{pixels} \tag{2.49}$$

Even after accounting for the CCD on SST being spatially under-sampled by a factor of 120, a $\frac{2111}{120} = 17.6$ pixel squared region on the actual detector is still more than large enough to contain a well-behaved PSF.

Shifting focus back to the binomial approximation of $r_{01}(u+u', v+v', \xi, \eta)$, (2.27) may be split into three terms as shown in (2.50).

$$r_{01}(u+u', v+v', \xi, \eta) \approx r_{01}(u, v, \xi, \eta) + \frac{u'^2 + v'^2}{2r_{01}(u, v, \xi, \eta)} - \frac{\xi' u' + \eta' v'}{r_{01}(u, v, \xi, \eta)} \tag{2.50}$$

Substituting (2.50) into (2.16) results in (2.51).

$$U\left(u+u',v+v'\right)=$$
$$\frac{1}{j\lambda z_{21}z_{01}}\iint A\left(\xi,\eta\right)\mathrm{e}^{jk\left(r_{21}(x,y,\xi,\eta)+r_{01}(u,v,\xi,\eta)+t(\xi,\eta)\right)}\,\mathrm{e}^{jk\left(\frac{u'^2+v'^2}{2r_{01}(u,v,\xi,\eta)}-\frac{\xi'u'+\eta'v'}{r_{01}(u,v,\xi,\eta)}\right)}d\xi d\eta \tag{2.51}$$

The quadratic phase term in (2.51) can be bounded above by replacing $r_{01}(u,v,\xi,\eta)$ with z_{01} as shown in (2.52), since $r_{01}(u,v,\xi,\eta)\geq z_{01}$.

$$\frac{u'^2+v'^2}{2r_{01}(u,v,\xi,\eta)}\leq\frac{u'^2+v'^2}{2z_{01}} \tag{2.52}$$

Spatial detector plane coordinates are transformed into pixel coordinates using (2.36) and the result is bounded above by replacing n and m with $n_{\max}$.

$$\frac{\lambda^2 z_{01}\left(n^2+m^2\right)}{4D^2}\leq\frac{\lambda^2 z_{01}{n_{\max}}^2}{2D^2} \tag{2.53}$$

Since wavelength is squared in (2.53), it will be much smaller than 1, assuming (2.48) is satisfied, allowing the quadratic phase term in (2.51) to be disregarded, yielding (2.54).

$$U_D\left(u+u',v+v'\right)=\frac{1}{j\lambda z_{21}z_{01}}\iint A\left(\xi,\eta\right)\mathrm{e}^{j\phi(\xi,\eta)}\,\mathrm{e}^{-jk\left(\frac{\xi'u'+\eta'v'}{r_{01}(u,v,\xi,\eta)}\right)}d\xi d\eta \tag{2.54}$$

The propagation equation in (2.54) is nearly a Fourier transform except that the denominator of the Fourier kernel is a function of the variables of integration. To approximate (2.54) as a Fourier transform, the condition shown in (2.55) must be satisfied.

$$\left|k\left(\frac{\xi'u'+\eta'v'}{r_{01}(u,v,\xi,\eta)}-\frac{\xi'u'+\eta'v'}{z_{01}}\right)\right|<<1 \tag{2.55}$$

In a similar manner to (2.52), a simplified upper-bound for (2.55) is created by substituting z_{01} for $r_{01}(u,v,\xi,\eta)$ in the denominator on the LHS of (2.56).

$$\left|k\left(\xi'u'+\eta'v'\right)\left(\frac{r_{01}(u,v,\xi,\eta)}{r_{01}^2(u,v,\xi,\eta)}-\frac{z_{01}}{z_{01}^2}\right)\right| \le \left|k\left(\xi'u'+\eta'v'\right)\frac{r_{01}(u,v,\xi,\eta)-z_{01}}{z_{01}^2}\right| \tag{2.56}$$

In (2.58), the RHS of (2.56) is further simplified though another upper bound generated by substituting the binomial approximation for $r_{01}(u,v,\xi,\eta)$, shown in (2.57).

$$r_{01}(u,v,\xi,\eta) \approx z_{01}+\frac{\xi'^2+\eta'^2}{2z_{01}^2} \tag{2.57}$$

$$\left|k\left(\xi'u'+\eta'v'\right)\right|\left|\frac{r_{01}(u,v,\xi,\eta)-z_{01}}{z_{01}^2}\right| \le \left|k\left(\xi'u'+\eta'v'\right)\right|\left|\frac{\xi'^2+\eta'^2}{2z_{01}^3}\right| \tag{2.58}$$

Finally, the expression is simplified even further using yet another upper bound, created this time by transforming u',v' to pixel coordinates n,m and substituting $n_{\max}$ for n and $m,\frac{D}{2}$ for ξ' and η'.

$$\left|k\left(\xi'u'+\eta'v'\right)\right|\left|\frac{\xi'^2+\eta'^2}{2z_{01}^3}\right| \le \frac{\pi n_{\max}\left(D\right)^3}{4Dz_{01}^2} \tag{2.59}$$

Substituting for in which case the RHS of (2.59) becomes the LHS of (2.60).

$$\frac{\pi n_{\max}}{4f_{\#}^2}<1 \tag{2.60}$$

The inequality in (2.60) suggests that the field produced in the detector plane using the Fourier Transform approximation of the Rayleigh-Sommerfeld formula in (2.61) is valid in a region around the point of interest in the detector plane defined by the f-number of the optical system.

$$U_D\left(u+u',v+v'\right) = \frac{1}{j\lambda z_{21}z_{01}}\iint A(\xi,\eta)\,\mathrm{e}^{jk\left(r_{21}(x,y,\xi,\eta)+r_{01}(u,v,\xi,\eta)+t(\xi,\eta)\right)}\,\mathrm{e}^{-j\frac{2\pi}{\lambda z_{01}}\left(\xi'u'+\eta'v'\right)}\,d\xi d\eta \tag{2.61}$$

If (2.60) is satisfied, the Rayleigh-Sommerfeld formula may be approximated using (2.61). Dropping the constant outside of the integral in (2.61) gives us the RHS of (2.10). Ignoring the constant outside of the integral in (2.61) is generally accepted since it has no effect on the PSF, which is normalized to sum to one.

Simulating Frames of Data

Since the mapping between an object and its image, or intensity, $i\left(\Delta_u n, \Delta_v m\right)$, is modeled through a two-dimensional convolution with the PSF, frames of data can be simulated using (2.62) [10]. The term $o\left(\Delta_x w, \Delta_y s\right)$ represents the object, where Δ_x and Δ_y are spatial sampling periods and w, s are discrete object plane coordinates.

$$i\left(\Delta_u n, \Delta_v m\right) = \sum_{w,s} h\left(\Delta_u\left(n-w\right), \Delta_v\left(m-s\right)\right) o\left(\Delta_x w, \Delta_y s\right) \tag{2.62}$$

Spatial sampling periods are dropped throughout the rest of this Thesis in favor of compressed notation. The object, aperture, and detector planes instead of being continuous planes are redefined as two-dimensional arrays. Discrete coordinates address array elements in the same manner as the Cartesian system, where the center element of the array corresponds to the origin. Removing the spatial sampling periods from (2.62) yields (2.63).

$$i\left(n, m\right) = \sum_{w,s} h\left(n-w, m-s\right) o\left(w, s\right) \tag{2.63}$$

Images generated using (2.63) lack realism due to the absence of noise. In actual images, each pixel contains shot noise caused by the discrete nature of photons [11]. Shot noise is simulated by selecting intensity values for each pixel using the Poisson distribution

shown in (2.64), whose mean is the true intensity, $i(n,m)$, plus the background, B. The background accounts for all light captured by the detector not originating from the object. The final data frame is represented as $d(n,m)$ and P represents the probability.

$$P\left(d(n,m)\right) = \frac{e^{i(n,m)+B}\left(i(n,m)+B\right)^{d(n,m)}}{d(n,m)!} \tag{2.64}$$

Frames can be down-sampled by a factor of N by convolving the intensity with a square ones matrix of size N and decimating the result by N as shown in (2.65). Blurring and decimation are simultaneously accomplished by the term $b(Nn-\tilde{n}, Nm-\tilde{m})$, where b is a square ones matrix of size N and $\tilde{n},\tilde{m}$ are dummy detector plane coordinates.

$$i_{usamp}(n,m) = \sum_{\tilde{n},\tilde{m}} b(Nn-\tilde{n}, Nm-\tilde{m})\, i(\tilde{n},\tilde{m}) \tag{2.65}$$

Noise is added in the same manner as Nyquist-sampled frames using the Poisson distribution from (2.64).

Fourier transforms can be used to implement (2.62) and (2.65), as shown in (2.66) and (2.67). The operators F and F^{-1} represent the two-dimensional Discrete Fourier transform and its inverse.

$$i(n,m) = F^{-1}\left\{F\left\{h(n,m)\right\} F\left\{o(w,s)\right\}\right\} \tag{2.66}$$

$$\begin{aligned} i_{blurr}(n,m) &= F^{-1}\left\{F\left\{b(n,m)\right\} F\left\{i(n,m)\right\}\right\} \\ i_{dsamp}(n,m) &= i_{blurr}(Nn, Nm) \end{aligned} \tag{2.67}$$

When using Fourier transforms to down-sample, blurring and decimation must be performed in two separate steps as shown in (2.67). The term $i_{blurr}(n,m)$ represents the

blurred intensity and the term $i_{dsamp}(n,m)$ represents the down-sampled intensity. Using Fourier transforms as shown in (2.66) and (2.67) also requires all arrays to be the same size. Therefore, the blurring function is zero-padded to be the same size as the detector plane. Additionally, (2.66) and (2.67) implement circular convolution instead of linear convolution. However, the use of circular convolution is acceptable for astronomical images where the object only extends over a small portion of the center region of the image.

III. Under-sampled Blind Deconvolution

Since images produced by optical systems are modeled by convolving the PSF with the object being observed as shown in (2.66) and (2.67), the reverse process, deconvolution, can generate estimates of the PSF from data. Generally, both the PSF and the object are unknown and must be estimated jointly. Techniques to jointly estimate both the PSF and the true object intensity are called blind deconvolution algorithms. Schultz introduced a blind deconvolution algorithm for Nyquist-sampled astronomical images which is extended for use with under-sampled data in the following section [12]. All derivations in the remainder of this chapter are performed in one dimension to compress notation, but can be generalized to two.

Estimate Update Equations

Assuming an image is dominated by shot noise, the intensity measured by the υ^{th} pixel of data, $d(\upsilon)$, can be considered a Poisson random variable with the Probability MassFunction (PMF) shown in (3.1) [12].

$$P\left(d(\upsilon)\right) = \frac{e^{-i(\upsilon)+B}\left(i(\upsilon)+\mathrm{B}\right)^{d(\upsilon)}}{d(\upsilon)!} \tag{3.1}$$

The expected value of the υ^{th} pixel is the true intensity, $i(\upsilon)$, plus background, B (3.2).

$$E\left[d(\upsilon)\right] = i(\upsilon) + B \tag{3.2}$$

Independence is assumed for the intensity measurements of each pixel. Therefore, the likelihood function for the entire frame of data is the product of the PMFs for each pixel, (3.3) [12].

$$P(d)=\prod_{\upsilon}\frac{e^{-i(\upsilon)+\mathrm{B}}\left(i(\upsilon)+\mathrm{B}\right)^{d(\upsilon)}}{d(\upsilon)!} \tag{3.3}$$

Two sets of complete data, $\tilde{d}(\upsilon,\psi,\chi)$ and $\tilde{c}(\upsilon)$, are defined in (3.4), where $\tilde{d}(\upsilon,\psi,\chi)$ is related to $i(\upsilon)$ and $\tilde{c}(\upsilon)$ is related to B.

$$d(\upsilon)=\sum_{\psi}\sum_{\chi}\tilde{d}(\upsilon,\psi,\chi)+\tilde{c}(\upsilon) \tag{3.4}$$

If the expected values of the two sets of complete data are defined as in (3.5) the relationship between the measured data and true intensity in (3.2) is preserved, as shown in (3.6). The coordinates χ and ψ span the object and PSF, respectively.

$$\begin{aligned}E\left[\tilde{d}(\upsilon,\psi,\chi)\right]&=b(N\upsilon-\psi)h(\psi-\chi)o(\chi)\\ E\left[\tilde{c}(\upsilon)\right]&=C=\frac{B}{(\#\chi)(\#\psi)}\end{aligned} \tag{3.5}$$

In (3.5), $\#\chi$ and $\#\psi$ denote the cardinality of χ and ψ.

$$\begin{aligned}E\left[d(\upsilon)\right]&=\sum_{\psi}\sum_{\chi}E\left[\tilde{d}(\upsilon,\psi,\chi)+\tilde{c}(\upsilon)\right]=\sum_{\psi}\sum_{\chi}b(N\upsilon-\psi)h(\psi-\chi)o(\chi)+C\\ &=i(\upsilon)+\#\chi\#\psi C=i(\upsilon)+B\end{aligned} \tag{3.6}$$

Equations (3.8) and (3.9) confirm the PMFs of the complete data are consistent with the PDF of the measured data, (3.1), if the complete data are defined as independent Poisson random variables, as shown in (3.7).

$$\begin{aligned}P\left(\tilde{d}(\upsilon,\psi,\chi)\right)&=\frac{e^{-\left(b(N\upsilon-\psi)h(\psi-\chi)o(\chi)\right)}\left(b(N\upsilon-\psi)h(\psi-\chi)o(\chi)\right)^{\tilde{d}(\upsilon,\psi,\chi)}}{\tilde{d}(\upsilon,\psi,\chi)!}\\ P\left(\tilde{c}(\upsilon)\right)&=\frac{e^{-C}(C)^{\tilde{c}(\upsilon)}}{\tilde{c}(\upsilon)!}\end{aligned} \tag{3.7}$$

In (3.8) and (3.9), note that the addition of two independent Poisson random variables produces another Poisson random variable with mean equal to the sum of the means of the two original Poisson random variables.

$$P\left(\tilde{d}\left(\upsilon,\psi,\chi\right)+\tilde{c}\left(\upsilon\right)\right)=\frac{e^{-\left(b\left(N\upsilon-\psi\right)h\left(\psi-\chi\right)o\left(\chi\right)+C\right)}\left(b\left(N\upsilon-\psi\right)h\left(\psi-\chi\right)o\left(\chi\right)+C\right)^{\tilde{d}\left(\upsilon,\psi,\chi\right)+\tilde{c}\left(\upsilon\right)}}{\tilde{d}\left(\upsilon,\psi,\chi\right)+\tilde{c}\left(\upsilon\right)!} \quad (3.8)$$

$$\begin{aligned} P\left(d\left(\upsilon\right)\right) &= P\left(\sum_{\psi}\sum_{\chi}\left[\tilde{d}\left(\upsilon,\psi,\chi\right)+\tilde{c}\left(\upsilon\right)\right]\right) \\ &= \frac{e^{-\sum_{\psi}\sum_{\chi}\left[b\left(N\upsilon-\psi\right)h\left(\psi-\chi\right)o\left(\chi\right)+C\right]}\left(\sum_{\psi}\sum_{\chi}\left[b\left(N\upsilon-\psi\right)h\left(\psi-\chi\right)o\left(\chi\right)+C\right]\right)^{d\left(\upsilon\right)}}{d\left(\upsilon\right)!} \quad (3.9) \\ &= \frac{e^{-\left(i\left(\upsilon\right)+B\right)}\left(i\left(\upsilon\right)+\mathrm{B}\right)^{d\left(\upsilon\right)}}{d\left(\upsilon\right)!} \end{aligned}$$

The statistical model for the complete data is validated in (3.9), where the statistical model for the incomplete data is produced through the relationship between the incomplete data and the complete data defined in (3.1). Therefore, we move on to deriving the log-likelihood of the complete data in (3.10)-(3.12).

Since the two sets of complete data are independent, the joint PMF is a product of the individual PMFs.

$$P\left(\tilde{d}\left(\upsilon,\psi,\chi\right),\tilde{c}\left(\upsilon\right)\right)=\frac{e^{-\left(b\left(N\upsilon-\psi\right)h\left(\psi-\chi\right)o\left(\chi\right)\right)}\left(b\left(N\upsilon-\psi\right)h\left(\psi-\chi\right)o\left(\chi\right)\right)^{\tilde{d}\left(\upsilon,\psi,\chi\right)}}{\tilde{d}\left(\upsilon,\psi,\chi\right)!}\frac{e^{-C}\left(C\right)^{\tilde{c}\left(\upsilon\right)}}{\tilde{c}\left(\upsilon\right)!} \quad (3.10)$$

Therefore, assuming independence over υ, ψ, and χ the likelihood function of the complete data is the product of the joint PMF, (3.10), over υ, ψ, and χ as shown in (3.11).

$$P\left(\tilde{d}\left(\upsilon,\psi,\chi\right),\tilde{c}\left(\upsilon\right)\right)$$
$$=\prod_{\upsilon}\prod_{\psi}\prod_{\chi}\frac{e^{-\left(b\left(N\upsilon-\psi\right)h\left(\psi-\chi\right)o\left(\chi\right)\right)}\left(b\left(N\upsilon-\psi\right)h\left(\psi-\chi\right)o\left(\chi\right)\right)^{\tilde{d}\left(\upsilon,\psi,\chi\right)}}{\tilde{d}\left(\upsilon,\psi,\chi\right)!}\frac{e^{-C}\left(C\right)^{\tilde{c}\left(\upsilon\right)}}{\tilde{c}\left(\upsilon\right)!} \quad (3.11)$$

Taking the natural logarithm of (3.11) gives the log-likelihood of the complete data, (3.12).

$$\begin{aligned}L^{CD}=&-\sum_{\upsilon}\sum_{\psi}\sum_{\chi}b\left(N\upsilon-\psi\right)h\left(\psi-\chi\right)o\left(\chi\right)+C+\ln\left(\tilde{d}\left(\upsilon,\psi,\chi\right)!\tilde{c}\left(\upsilon\right)!\right)\\&+\sum_{\upsilon}\sum_{\psi}\sum_{\chi}\tilde{d}\left(\upsilon,\psi,\chi\right)\ln\left(b\left(N\upsilon-\psi\right)h\left(\psi-\chi\right)o\left(\chi\right)\right)+\tilde{c}\left(\upsilon\right)\ln\left(C\right)\end{aligned} \quad (3.12)$$

To derive the object and PSF updates, the Q function is defined as the expected value of the complete data likelihood based on data, the old object estimate, o^{old}, and the old PSF estimate, h^{old}, as shown in (3.13).

$$Q\equiv E^{old}\left[L^{CD}\mid d,o^{old},h^{old}\right] \quad (3.13)$$

Substituting the complete data log-likelihood function, (3.12), into (3.13) gives (3.14).

$$\begin{aligned}Q=&-\sum_{\upsilon}\sum_{\psi}\sum_{\chi}b\left(N\upsilon-\psi\right)h\left(\psi-\chi\right)o\left(\chi\right)+C+E^{old}\left[\ln\left(\tilde{d}\left(\upsilon,\psi,\chi\right)!\tilde{c}\left(\upsilon\right)!\right)\mid d\left(\upsilon\right)\right]\\&+\sum_{\upsilon}\sum_{\psi}\sum_{\chi}E^{old}\left[\tilde{d}\left(\upsilon,\psi,\chi\right)\mid d\left(\upsilon\right)\right]\ln\left(b\left(N\upsilon-\psi\right)h\left(\psi-\chi\right)o\left(\chi\right)\right)\\&+E^{old}\left[\tilde{c}\left(\upsilon\right)\mid d\left(\upsilon\right)\right]\ln\left(C\right)\end{aligned} \quad (3.14)$$

An expression for $E^{old}\left[\tilde{d}\left(\upsilon,\psi,\chi\right)\mid d\left(\upsilon\right)\right]$ is derived in (3.16)-(3.21). To compress notation, the substitutions shown in (3.15) are made.

$$\begin{aligned}\tilde{d}&=\tilde{d}\left(\upsilon,\psi,\chi\right)\\d&=d\left(\upsilon\right)\end{aligned} \quad (3.15)$$

The probability distribution, $P\left(\tilde{d}\mid d\right)$ is derived using Bayes' theorem in (3.16).

$$P\left(\tilde{d} \mid d\right) = \frac{P\left(\tilde{d}, d\right)}{P\left(d\right)} \tag{3.16}$$

The joint PMF of the complete and measured data can be found using (3.17), due to the definition of the complete data, (3.4).

$$P\left(\tilde{d}, d\right) = P\left(\tilde{d}\right) P\left(d - \tilde{d}\right) \tag{3.17}$$

Substituting Poisson PMFs on the right-hand side (RHS) of (3.17) gives (3.18).

$$P\left(\tilde{d}, d\right) = \frac{E\left[\tilde{d}\right]^{\tilde{d}} e^{-E\left[\tilde{d}\right]}}{\tilde{d}!} \frac{E\left[d - \tilde{d}\right]^{d-\tilde{d}} e^{-E\left[d-\tilde{d}\right]}}{\left(d - \tilde{d}\right)!} \tag{3.18}$$

The PMF for the measured data is shown in (3.19).

$$P\left(d\right) = \frac{E\left[d\right]^{d} e^{-E[d]}}{\left(d\right)!} \tag{3.19}$$

Substituting (3.19) and (3.18) into (3.16) gives (3.20), which is the equation for a binomial probability density function with number of trials d and probability of success $\frac{E\left[\tilde{d}\right]}{E\left[d\right]}$.

$$P\left(\tilde{d} \mid d\right) = \frac{(d)!}{\tilde{d}!\left(d - \tilde{d}\right)!} \left(\frac{E\left[\tilde{d}\right]}{E\left[d\right]}\right)^{\tilde{d}} \left(\frac{E\left[d - \tilde{d}\right]}{E\left[d\right]}\right)^{d-\tilde{d}} \tag{3.20}$$

Taking the expectation of (3.20) and substituting (3.5) and (3.2) produces the final expression for $E^{old}\left[\tilde{d}\left(\upsilon, \psi, \chi\right) \mid d\left(\upsilon\right)\right]$ in (3.21), where $i^{old}\left(\upsilon\right)$, refers to the old intensity estimate.

$$
\begin{aligned}
E^{old}\left[\tilde{d}(\upsilon,\psi,\chi)\,|\,d(\upsilon)\right] &= d\,\frac{E^{old}\left[\tilde{d}\right]}{E^{old}\left[d\right]} \\
&= d(\upsilon)\frac{b(N\upsilon-\psi)h^{old}(\psi-\chi)\mathrm{o}^{old}(\chi)}{i^{old}(\upsilon)+B}
\end{aligned}
\tag{3.21}
$$

Substituting (3.21) into (3.14) results in (3.22).

$$
\begin{aligned}
Q = &-\sum_{\upsilon}\sum_{\psi}\sum_{\chi} b(N\upsilon-\psi)h(\psi-\chi)o(\chi) + C + E^{old}\left[\ln\left(\tilde{d}(\upsilon,\psi,\chi)!\tilde{c}(\upsilon)!\right)\,|\,d(\upsilon)\right] \\
&+\sum_{\upsilon}\sum_{\psi}\sum_{\chi} d_k(\upsilon)\frac{b(N\upsilon-\psi)h^{old}(\psi-\chi)\mathrm{o}^{old}(\chi)}{i^{old}(\upsilon)+B}\ln\left(b(N\upsilon-\psi)h(\psi-\chi)o(\chi)\right) \\
&+E^{old}\left[\tilde{c}(\upsilon)\,|\,d(\upsilon)\right]\ln(C)
\end{aligned}
\tag{3.22}
$$

To determine the update equation for the object, Q is maximized by setting the derivative of (3.22) with respect to the object at an arbitrary point, $\mathrm{o}(\chi')$ to zero

$$
\begin{aligned}
\frac{\partial Q}{\partial\,\mathrm{o}(\chi')} = &-\sum_{\upsilon}\sum_{\psi}\sum_{\chi}\left(b(N\upsilon-\psi)h(\psi-\chi)\delta(\chi-\chi')\right) \\
&+\sum_{\upsilon}\sum_{\psi}\sum_{\chi} d(z)\frac{b(N\upsilon-\psi)h^{old}(\psi-\chi)\mathrm{o}^{old}(\chi)}{i^{old}(\upsilon)+B}\frac{\delta(\chi-\chi')}{o(\chi)}
\end{aligned}
\tag{3.23}
$$

The term $E^{old}\left[\ln\left(\tilde{d}(\upsilon,\psi,\chi)!\right)\,|\,\mathrm{d}(\upsilon)\right]$ disappears, as it only depends on $\mathrm{o}^{old}(\chi)$, and not $\mathrm{o}(\chi)$. Additionally, $E^{old}\left[\tilde{c}(\upsilon)\,|\,d(\upsilon)\right]\ln(C)$ and C vanish, since they are also constant with respect to $\mathrm{o}(\chi)$.

$$
\begin{aligned}
&\frac{\partial}{\partial\,\mathrm{o}(\chi')}E^{old}\left[\ln\left(\tilde{d}(\upsilon,\psi,\chi)!\right)\,|\,\mathrm{d}(\upsilon)\right] = 0 \\
&\frac{\partial}{\partial\,\mathrm{o}(\chi')}E^{old}\left[\tilde{c}(\upsilon)\,|\,d(\upsilon)\right]\ln(C) = 0 \\
&\frac{\partial}{\partial\,\mathrm{o}(\chi')}C = 0
\end{aligned}
\tag{3.24}
$$

Using the sifting rule, (3.23) becomes

$$\frac{\partial Q}{\partial \mathrm{o}(\chi')} = -\sum_{\upsilon}\sum_{\psi}\left(b(N\upsilon-\psi)h(\psi-\chi')\right) + \sum_{\upsilon}\sum_{\psi} d(\upsilon)\frac{b(N\upsilon-\psi)h^{old}(\psi-\chi')\mathrm{o}^{old}(\chi')}{i^{old}(\upsilon)+B}\frac{1}{\mathrm{o}(\chi')} \tag{3.25}$$

Setting the derivative of the Q function in (3.25) to zero and moving the negative term to the left-hand side (LHS) produces

$$\sum_{\upsilon}\sum_{\psi} b(N\upsilon-\psi)h(\psi-\chi') = \sum_{\upsilon}\sum_{\psi} d(\upsilon)\frac{b(N\upsilon-\psi)h^{old}(\psi-\chi')\mathrm{o}^{old}(\chi')}{i^{old}(\upsilon)+B}\frac{1}{\mathrm{o}(\chi')} \tag{3.26}$$

Isolating $\mathrm{o}(\mathrm{x}')$ in (3.26) on the RHS and moving $\mathrm{o}^{old}(\mathrm{x}')$ to the outside of the summation gives the update equation for object,

$$\mathrm{o}(\chi') = \mathrm{o}^{old}(\chi')\frac{\sum_{\upsilon}\sum_{\psi} d(\upsilon)\frac{b(N\upsilon-\psi)h^{old}(\psi-\chi')}{i^{old}(\upsilon)+B}}{\sum_{\upsilon}\sum_{\psi} b(N\upsilon-\psi)h(\psi-\chi')} \tag{3.27}$$

The PSF is constrained to sum to 1 as shown in (3.28). Additionally, the under-sampling function, b, also sums to 1 since decimating a square ones matrix of size N by a factor of N reduces to a single-element ones matrix.

$$\sum_{\psi} h(\psi) = 1 \qquad \sum_{\upsilon} b(N\upsilon) = 1 \tag{3.28}$$

Thus, the denominator on the RHS of (3.27) evaluates to

$$\sum_{\upsilon}\sum_{\psi} b(N\upsilon-\psi)h(\psi-\chi) = 1 \tag{3.29}$$

Substituting (3.29) into (3.27) produces the final object update equation.

$$\mathrm{o}(\chi') = \mathrm{o}^{old}(\chi') \sum_{\upsilon} \sum_{\psi} d(\upsilon) \frac{b(N\upsilon - \psi) h^{old}(\psi - \chi')}{i^{old}(\upsilon) + B} \tag{3.30}$$

The PSF update equation is derived in a similar manner to the object update equation, beginning by taking the derivative of the Q function with respect to an arbitrary point ψ' of the PSF, $h(\psi')$.

$$\begin{aligned} \frac{\partial Q}{\partial h(\psi')} = & -\sum_{\upsilon} \sum_{\psi} \sum_{\chi} \left(b(N\upsilon - \psi) o(\chi) \delta(\psi - \chi - \psi') \right) \\ & + \sum_{\upsilon} \sum_{\psi} \sum_{\chi} d(\upsilon) \frac{b(N\upsilon - \psi) h^{old}(\psi - \chi) \mathrm{o}^{old}(\chi)}{i^{old}(\upsilon) + B} \frac{\delta(\psi - \chi - \psi')}{h(\psi - \chi - \psi')} \end{aligned} \tag{3.31}$$

Note that the terms that vanished in (3.23) also vanish in (3.31). Using the sifting property results in

$$\begin{aligned} \frac{\partial Q}{\partial h(\psi')} = & -\sum_{\upsilon} \sum_{\psi} \left(b(N\upsilon - \psi) o(\psi - \psi') \right) \\ & + \sum_{\upsilon} \sum_{\psi} d(\upsilon) \frac{b(N\upsilon - \psi) \mathrm{o}^{old}(\psi - \psi') h^{old}(\psi')}{i^{old}(\upsilon) + B} \frac{1}{h(\psi')} \end{aligned} \tag{3.32}$$

Setting the derivative of the Q function in (3.32) to zero and moving the negative term to the LHS produces (3.33).

$$\begin{aligned} & \sum_{\upsilon} \sum_{\psi} b(N\upsilon - \psi) o(\psi - \psi') = \\ & \qquad \sum_{\upsilon} \sum_{\psi} d(\upsilon) \frac{b(N\upsilon - \psi) \mathrm{o}^{old}(\psi - \psi') h^{old}(\psi')}{i^{old}(\upsilon) + B} \frac{1}{h(\psi')} \end{aligned} \tag{3.33}$$

Isolating $h(\chi')$ on the LHS and moving $h^{old}(\chi')$ outside of the summation gives the update equation for the PSF (3.34).

$$h(\psi') = h^{old}(\psi') \frac{\sum_{\upsilon}\sum_{\psi} d(\upsilon) \frac{b(N\upsilon - \psi)\,\mathrm{o}^{old}(\psi - \psi')}{i^{old}(\upsilon) + B}}{\sum_{\upsilon}\sum_{\psi} b(N\upsilon - \psi)\, o(\psi - \psi')} \tag{3.34}$$

Since the blurring function is defined to sum to one (3.28), the summation in the denominator of the PSF update equation, (3.34), is equivalent to summing over the object, which gives constant K in (3.35).

$$\sum_{\upsilon}\sum_{\psi} b(N\upsilon - \psi)\, o(\psi - \psi') = \sum_{\psi} o(\psi - \psi') = \sum_{\psi} o(\psi) = K \tag{3.35}$$

Substituting (3.35) into (3.34) gives (3.36).

$$h(\psi') = h^{old}(\psi') \frac{\sum_{\upsilon}\sum_{\psi} d(\upsilon) \frac{b(N\upsilon - \psi)\,\mathrm{o}^{old}(\psi - \psi')}{i^{old}(\upsilon) + B}}{K} \tag{3.36}$$

The PSF was defined to sum to one in (3.28). Therefore, when updating the PSF, the constant in the denominator of (3.36) is ignored and the updated PSF is normalized to sum to one as shown in (3.37).

$$\begin{aligned} h(\psi') &= h^{old}(\psi') \sum_{\upsilon}\sum_{\psi} d(\upsilon) \frac{b(N\upsilon - \psi)\,\mathrm{o}^{old}(\psi - \psi')}{i^{old}(\upsilon) + B} \\ h^{new}(\psi') &= \frac{h(\psi')}{\sum_{\psi'} h(\psi')} \end{aligned} \tag{3.37}$$

Computationally, Fourier transforms are used to implement the estimate update equations as shown in (3.38) and (3.39), where $*$ denotes a conjugation.

$$h(\psi') = h^{old}(\psi') F^{-1}\left\{ F\left\{ \frac{d(\upsilon)}{i^{old}(\upsilon) + B} \right\} \left(F\{b(\upsilon)\} F\left\{ \mathrm{o}^{old}(\chi) \right\}^{*} \right)^{*} \right\} \tag{3.38}$$

$$\mathrm{o}(\chi') = \mathrm{o}^{old}(\chi') F^{-1}\left\{ F\left\{ \frac{d(\upsilon)}{i^{old}(\upsilon) + B} \right\} \left(F\{b(\upsilon)\} F\left\{ h^{old}(\psi) \right\}^{*} \right)^{*} \right\} \tag{3.39}$$

Although computationally more efficient, there are drawbacks to using Fourier transforms to compute update equations. One issue is that circular convolution is implemented instead of linear convolution. Using circular convolution instead of linear convolution is acceptable for astronomical images of near-point sources where only background noise is present at the edges of the image. Zero-padding must be performed for images with significant content near the edges. Another inconvenience is that all matrices must be the same size. Therefore, to recover a Nyquist-sampled PSF, the data must be up-sampled by a factor of N before being used in the update equations. The blurring function must be zero-padded to match the PSF array size.

Updating PSF and object estimates using (3.38) and (3.39) guarantees the likelihood will increase every iteration [13]. However, estimates converge to a trivial solution if left unconstrained, where the object becomes a point source and the PSF becomes the data. One method Shultz proposed to overcome the trivial solution was to incorporate a phase-retrieval algorithm called Gerchberg-Saxton into blind-deconvolution to prevent the PSF from converging to the data [12]. The phase retrieval algorithm described in this thesis uses similar approach where the PSF is constrained using the phase retrieval algorithm.

Termination Condition

Using the Cramer-Rao lower bound, the minimum variance between a parameter and its estimate can be estimated by inverting the Fisher information matrix as shown in (3.40), where $\mathrm{cov}(\theta)$ is the covariance matrix of the estimated parameters, θ, and $\mathbf{I}$ represents the Fisher information matrix [14].

$$\mathrm{cov}\left(\theta\right) \geq \mathbf{I}^{-1} \tag{3.40}$$

Entry γ,ς of the Fisher information matrix is defined as shown in (3.41) [14].

$$I_{\gamma\varsigma} = -E\left[\frac{\partial^2 L}{\partial\theta_\gamma \partial\theta_\varsigma}\right] \tag{3.41}$$

The log-likelihood function, L, for a single frame of data is shown in (3.42), where $i(\upsilon)$ is the true intensity and $d(\upsilon)$ is the captured frame of data.

$$L = \sum_{\upsilon}\left[-\left(i(\upsilon)+B\right)+d(\upsilon)\ln\left(i(\upsilon)+B\right)-\ln\left(d(\upsilon)!\right)\right] \tag{3.42}$$

Since the true intensity is being estimated, $\theta = i$ and the Fisher information matrix can be found by first taking the derivative of (3.42) with respect to $i(\gamma)$.

$$\frac{\partial L}{\partial i(\gamma)} = -1+\frac{\mathrm{d}(\gamma)}{i(\gamma)+B} \tag{3.43}$$

The second derivative is now taken with respect to the true intensity. The second derivative is equal to zero except when the second derivative is taken with respect to the same pixel as the first derivative, as shown in (3.44).

$$\frac{\partial^2 L}{\partial i(\gamma)\partial i(\varsigma)} = \begin{cases} -\dfrac{\mathrm{d}(\gamma)}{\left(i(\gamma)+\mathrm{B}\right)^2} & \gamma=\varsigma \\ 0 & \gamma\neq\varsigma \end{cases} \tag{3.44}$$

Therefore, the Fisher information matrix is a diagonal matrix as shown below.

$$I_{\gamma\varsigma} = \begin{cases} \dfrac{1}{i(\gamma)+\mathrm{B}} & \gamma=\varsigma \\ 0 & \gamma\neq\varsigma \end{cases} \tag{3.45}$$

Inverting a diagonal matrix is equivalent to inverting each of its elements. Therefore the lower bound for variance is equal to the value of the corresponding true intensity pixel.

$$\mathrm{var}\left(i(\gamma)\right) \geq i(\gamma) + \mathrm{B} \tag{3.46}$$

When using only a single frame of data, the blind deconvolution algorithm is thus terminated when the sum of squared error between the intensity estimate and the data is less than or equal to sum of the data. This convergence of variance termination condition was used by Neff in his work to estimate seeing conditions [15].

IV. Phase Retrieval

Phase retrieval is the process of recovering phase from intensity measurements. Phase retrieval is widely applicable in optical sensing problems because intensity is often the only directly measurable quantity. To determine the aberrations that are present in the system, the phase of the field must be retrieved. The phase retrieval technique reported in this research is based on Blind-deconvolution, Gerchberg-Saxton, and a field-based compass search. Blind deconvolution was described in the previous chapter as a means of separating the object from the PSF. The Gerchberg-Saxton algorithm and the Field-based compass search are explained in the first two sections of this chapter, which concludes by described in the phase retrieval algorithm in its third and final section.

Gerchberg-Saxton

The Gerchberg-Saxton (GS) algorithm was one of the first successful algorithms developed for phase retrieval. The field function, $\Phi(p,q)$, is defined as

$$\Phi(p,q) = A(p,q)e^{j\phi(p,q)} \tag{4.1}$$

The magnitude of the field function and the detector field is known to be the aperture and the square root of the PSF respectively [7]. The field function in (4.1) is equal to the argument of the Fourier propagation from (2.10) and (2.11). The GS algorithm exploits the Fourier relationship between the field function and the detector field by iteratively constraining the magnitude of the two fields while allowing their phase to change. As shown in (4.2), the constrained field function estimate, $\tilde{\Phi}(p,q)$, may be initialized to any field, as long as its magnitude is consistent with the aperture shape.

$$\left|\tilde{\Phi}(p,q)\right| = A(p,q) \tag{4.2}$$

First, the unconstrained detector field estimate, $\hat{U}_D(n,m)$, is updated to the Fourier transform of the constrained phase function estimate [7].

$$\hat{U}_D(n,m) = F\left\{\tilde{\Phi}(p,q)\right\} \tag{4.3}$$

Then, the magnitude of the detector field estimate is constrained to the square root of the point-spread function [7].

$$\tilde{U}_D(n,m) = \sqrt{h(n,m)}\left(\frac{\hat{U}_D(n,m)}{\left\|\hat{U}_D(n,m)\right\|}\right) \tag{4.4}$$

Next, the estimated field function is updated the inverse Fourier transform of the constrained detector field [7].

$$\hat{\Phi}(p,q) = F\left\{\tilde{U}_D(n,m)\right\}^{-1} \tag{4.5}$$

Finally, the magnitude of the field function is constrained to the aperture shape [7].

$$\tilde{\Phi}(p,q) = A(p,q)\left(\frac{\hat{\Phi}(p,q)}{\left\|\hat{\Phi}(p,q)\right\|}\right) \tag{4.6}$$

Steps (4.3)-(4.6) are iteratively repeated until a loop limit is exceeded to improve the field estimate, as shown in Figure 5 [7].

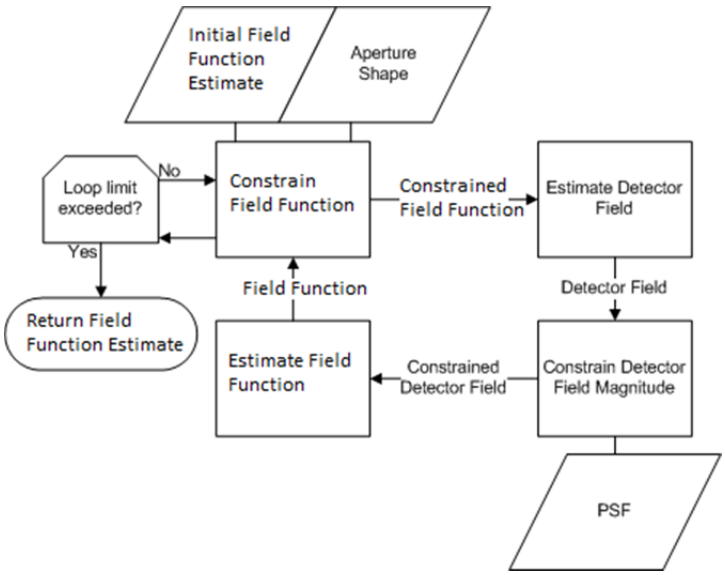

Figure 5: Gerchberg Saxton (GS).

Every iteration of the GS algorithm reduces the error between the true and estimated fields. However, convergence to the true field is not guaranteed.

Compass Search

The compass search is a subset of direct search algorithms, which are not gradient-based. Gradient-based algorithms are faster but their use is avoided due to their susceptibility to noise [16]. The compass search was also utilized by Zingarelli [9]. At each iteration, the compass search moves one of the current parameter estimates in the direction that produces the most favorable objective function value [16]. Every estimated parameter is considered a separate dimension in the search space [16]. The objective function is evaluated for every possible axial direction of movement and the current parameter set is moved in the direction that produces the most favorable value [16]. A two-dimensional compass search is illustrated in Figure 6.

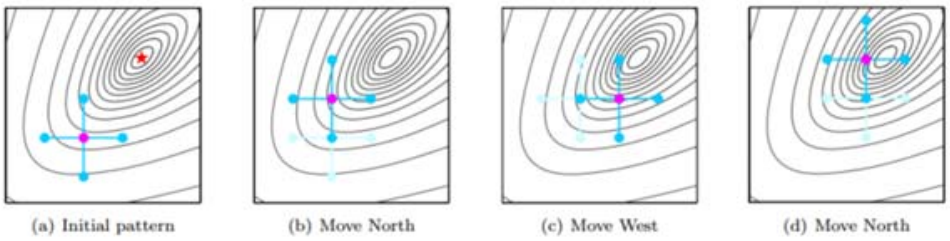

Figure 6: Two-dimensional compass search.

The Field-based compass search is shown in Figure 7, where Zernike coefficients 2 through 11 are fitted to the field recovered by the GS algorithm. The search space is ten-dimensional, where each dimension defined by a single Zernike coefficient.

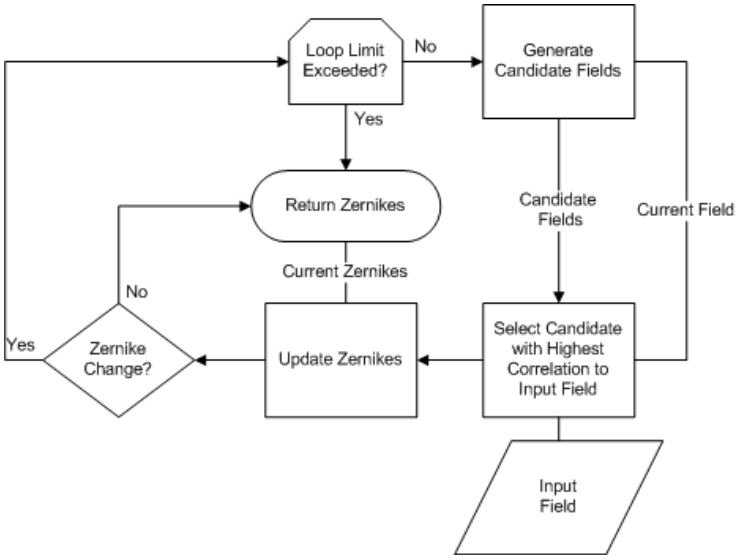

Figure 7: Field-based compass search.

The objective function is defined by the correlation, $\Gamma(a)$, between the field function estimate produced by GS, $\Phi_{gs}(p,q)$, and the field produced by one of the a potential Zernike coefficient estimate updates, $\Phi_{zern}^{a}(p,q)$.

$$\Gamma(a) = \frac{\sum_p \sum_q \mathrm{Re}\left\{ \Phi_{gs}(p,q) \Phi^a_{zern}(p,q)^* \right\}}{\sum_p \sum_q A(p,q)} \tag{4.7}$$

In (4.7), $\mathrm{Re}\{\ \}$ returns the real portion of its argument. The coefficient estimates are moved in the direction of highest correlation, which implies a better estimate.

Phase Retrieval Algorithm

Blind-deconvolution, GS, and Field-based compass search are combined into the phase retrieval algorithm shown in Figure 8.

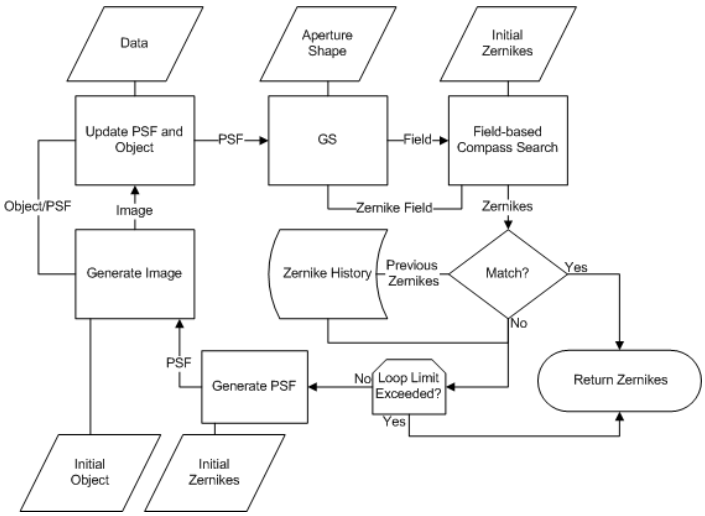

Figure 8: Field-based phase retrieval

As input, phase retrieval algorithm requires data, aperture shape, initial Zernike coefficients and an initial object estimate. First, the intensity estimate is generated based on object and Zernike estimates using (2.1)-(2.5) and (2.62). The object and PSF are updated based on blind-deconvolution update equations (3.38) and (3.39). The updated PSF is input into the GS algorithm, whose aperture field is initialized based on current Zernike estimates, $\hat{\alpha}_i$.

$$\tilde{\Phi}(p,q) = A(p,q)e^{j\sum_{i=2}^{11}\hat{\alpha}_i Z_i(p,q)} \tag{4.8}$$

After the GS algorithm is executed for a number of iterations, the field produced by GS is passed to the field-based compass search algorithm. The field-based search updates Zernike coefficient estimates using the field produced by GS, then passes the Zernike-based field estimate back to GS as the initial aperture field for the next iteration of the phase retrieval algorithm. Zernikes are compared to a history of Zernike coefficients from previous iterations. The algorithm is terminated when all Zernikes coefficients in the history match. Using a history of Zernike estimates ensures that both the PSF and object estimates have stabilized before the algorithm is terminated.

Performance can be improved by running the phase retrieval algorithm multiple times with different starting points, as shown in Figure 9. The algorithm returns the Zernike estimate that generates the PSF yielding the smallest error between the data and the estimated intensity. Alternatively, the termination condition from Chapter 3 may be used return Zernike coefficient estimates immediately once convergence of variance is satisfied..

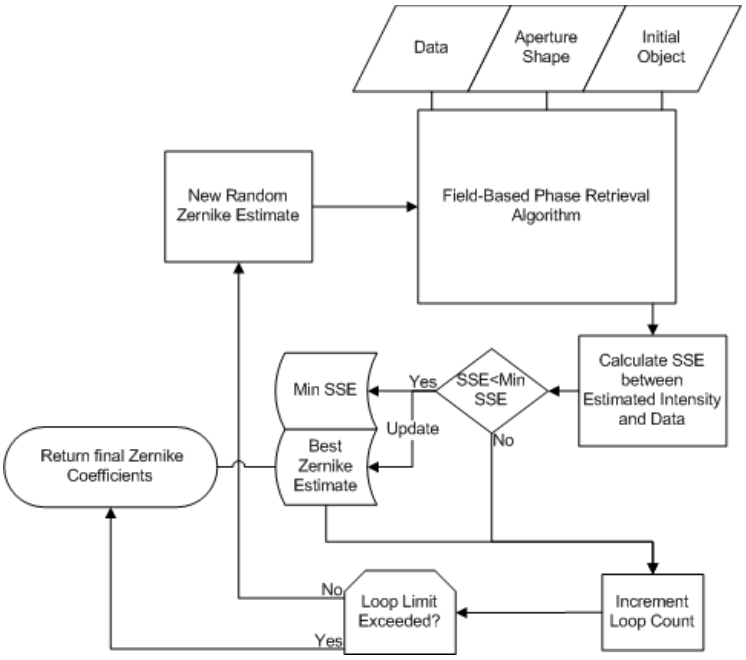

Figure 9: Field-based phase retrieval with random starting points.

V. Simulation/Experimentation and Results

Number of Gerchberg-Saxton Iterations

A simulation was conducted to determine the number of iterations of GS to perform within the phase retrieval algorithm. The GS algorithm was executed on 100 different PSFs, generated by randomly choosing Zernike coefficients 2 through 11 from a normal distribution. For each instance, the initial aperture phase was initialized to the aperture itself, and the squared error between the true and estimated PSF was tracked for 100 iterations. Figure 10 shows the average squared error curve.

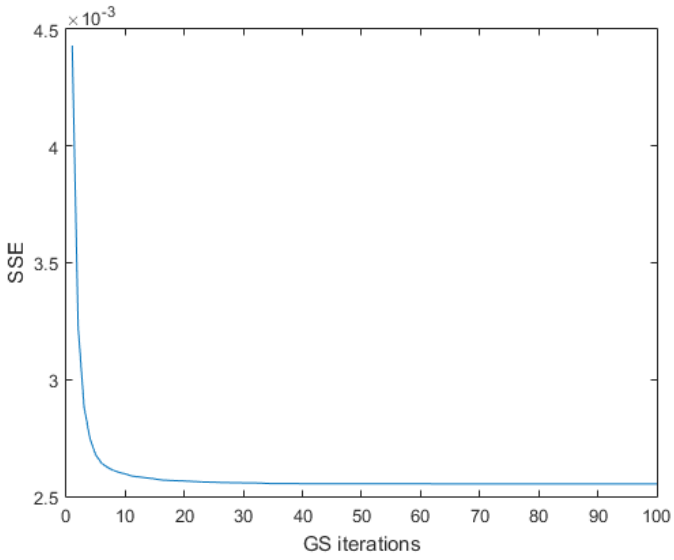

Figure 10: Reduction in squared error from GS iterations.

Performing more than 10 iterations of GS does not significantly reduce the squared error between the true and estimated PSF. Therefore, 10 iterations of GS are preformed within the phase retrieval algorithm.

Random Zernike Simulation

The performance of the phase retrieval algorithm was evaluated using simulated frames of data, generated using (2.62)-(2.65). Zernike coefficients were randomly selected from a normal distribution. Frames were simulated for a point-source object with intensity 10e4 photons and 1 photon of background. Figure 11 shows simulated Nyquist-sampled and under-sampled data. True intensity is shown in the top row and the final, simulated frame with shot noise is shown in the bottom row. The left column of Figure 11 is Nyquist-sampled and the right column is under-sampled by a factor 2.

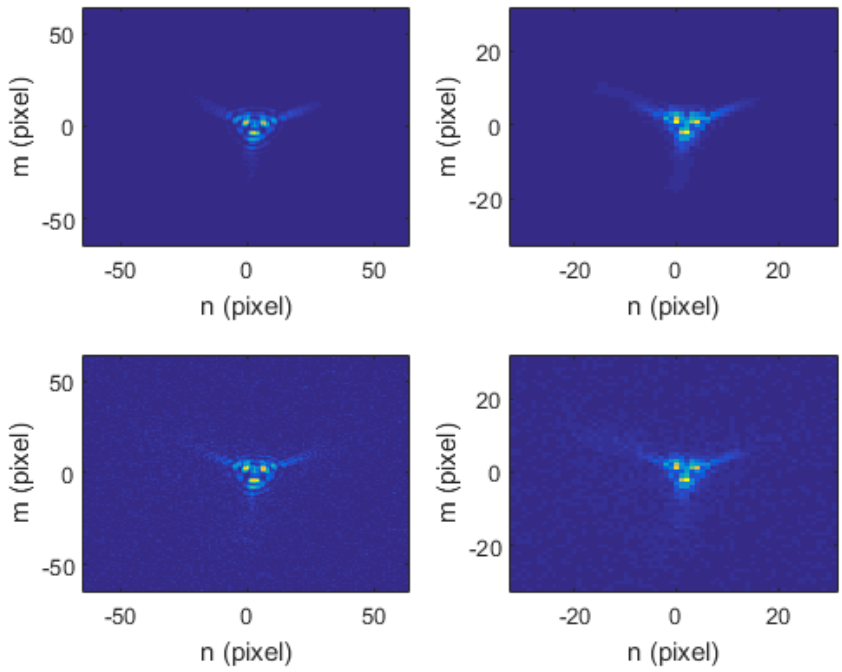

Figure 11: Simulated Data

In Figure 12, the zero-padded blurring function $b(n,m)$ is shown on the left and the under-sampled data after up-sampling is shown on the right.

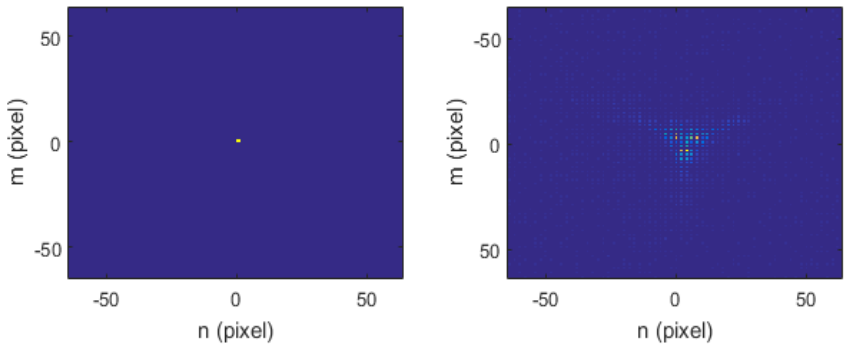

Figure 12: Under-sampled phase retrieval inputs. Blurring function (left), up-sampled data (right).

The object estimate is initialized to the zero-padded 5 by 5 ones matrix shown in Figure 13.

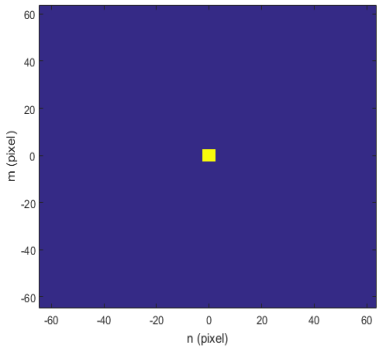

Figure 13: Initial object estimate.

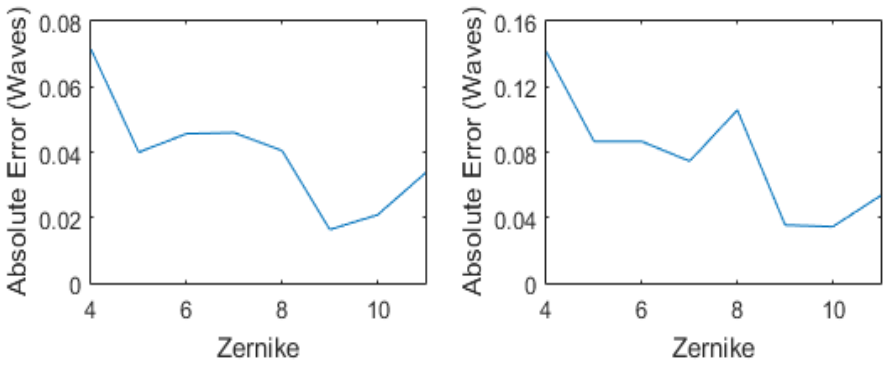

Figure 14: Simulation Results from 100 frames of simulated data. Absolute error between true and estimated Zernikes are plotted for results from Nyquist-sampled data (left), and data under-sampled by 2 (right).

Simulation results are shown in Figure 14. Tip and tilt were ignored because they are affected by the object estimate. The object estimate often converges to an off-axis point source, causing tip and tilt to compensate by straying from their true values. Ten iterations of the phase retrieval algorithm with randomly selected initial Zernikes were performed for each of the 100 simulated frames. Figure 14 shows the mean absolute error between the true and estimated Zernike coefficients. Results from Nyquist-sampled data are shown on the left while results from under-sampled data are shown on the right.

Defocus Experiment

A Newtonian telescope was used to observe a pinhole 15m away. The setup of the experiment is shown in Figure 15.

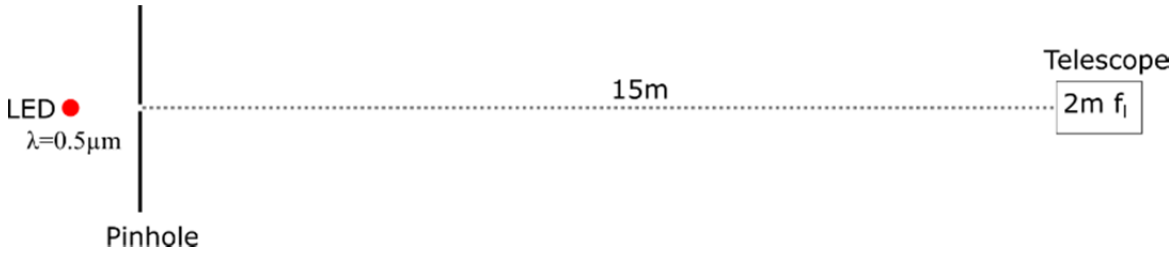

Figure 15: Defocus experiment setup.

The telescope was intentionally slightly defocused by an unknown amount. To obtain Nyquist-sampled and under-sampled data, the telescope aperture was setup as shown in Figure 16. An opaque screen was used to block out most of the original aperture around an adjustable iris. Spatial Nyquist-sampling in the detector plane for a circular aperture is defined by the relationship in (5.1), where dx is the pixel pitch.

$$dx = \frac{\lambda z}{2D} \tag{5.1}$$

The pixel pitch of the detector used in the experiment was 16μm. Therefore, assuming the change in focal length, z, to slightly defocus the telescope was insignificant, the aperture diameter D required for Nyquist-sampling was 3 cm as shown in (5.2).

$$D = \frac{\lambda z}{2dx} = \frac{.5\,\mu m(200\,cm)}{2(16\,\mu m)} = \frac{100\,cm}{32} \approx 3\,cm \tag{5.2}$$

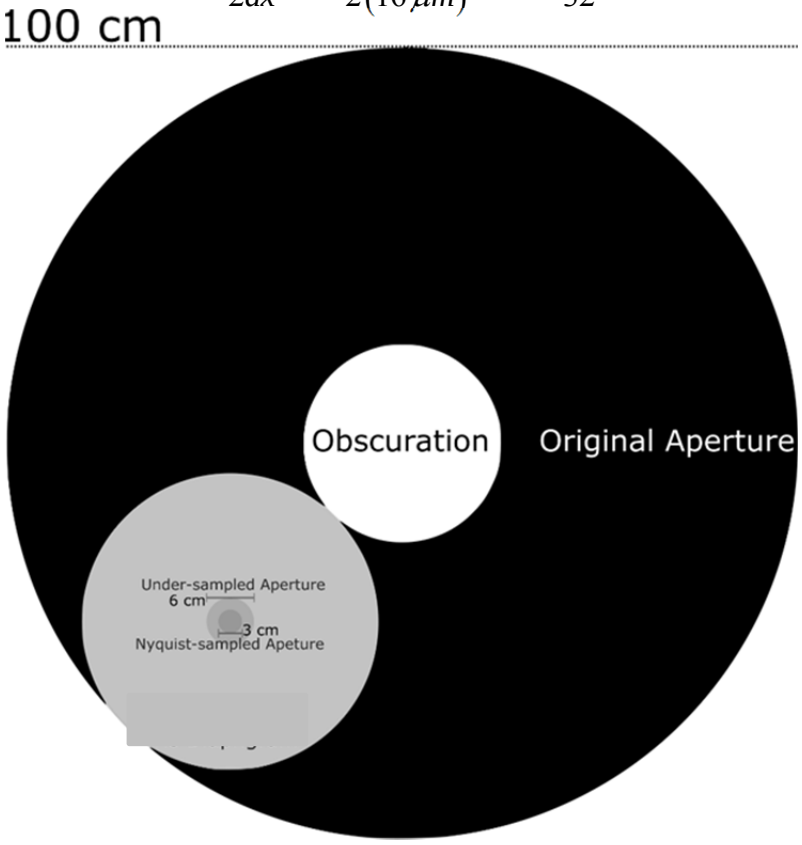

Figure 16: Telescope aperture.

Therefore, the effective aperture size of the telescope was reduced to 3 cm, as shown in Figure 16, to obtain a Nyquist-sampled image. The size of the aperture was then doubled to 6 cm to generate an image under-sampled by a factor of 2. Frames of data obtained from the experiment are shown in the top row of Figure 17. The corresponding PSFs recovered by the phase retrieval algorithm are shown in the bottom row. The initial object estimate in Figure 13 was used and the phase retrieval algorithm was executed 100 times

with initial sets of Zernike coefficients 2-11 randomly selected from a normal distribution.

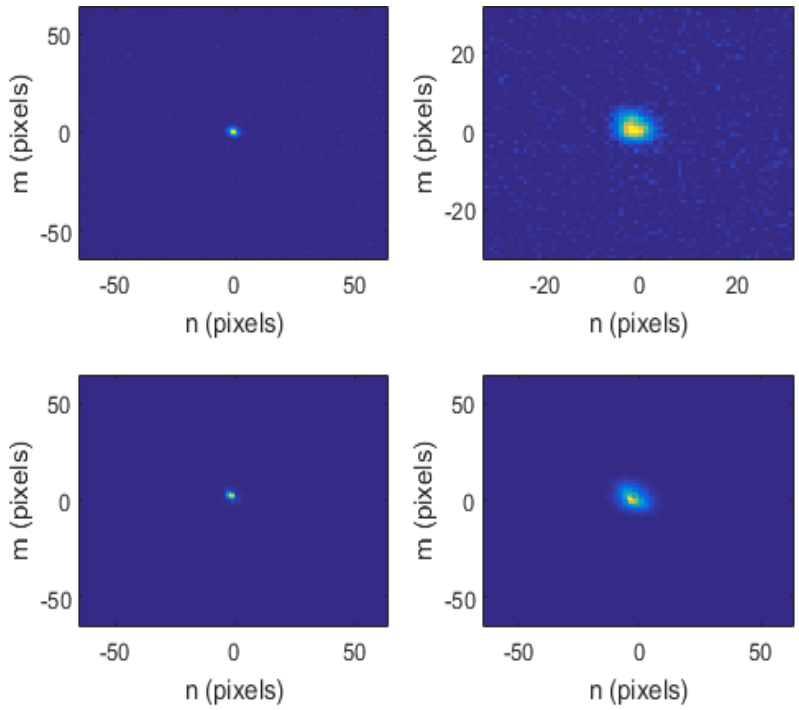

Figure 17: Defocus experiment results. Experiment data (top row), recovered PSFs (bottom row), Nyquist (left), under-sampled by 2 (right).

The final Zernike coefficient estimates minimizing the squared error between estimated intensity and the data is shown in Table 1.

Table 1: Recovered Zernike Coefficient Magnitudes

	Z4	Z5	Z6	Z7	Z8	Z9	Z10	Z11
Nyquist-sampled	0.31	0.06	0.04	0.02	0.17	0.07	0.02	0.47
Under-sampled	1.88	0.20	0.03	0.08	0.05	0.08	0.07	0.25

The recovered coefficients cannot be compared directly, because adjusting the aperture size affects the Zernike coefficients. The change in Zernike coefficients can be predicted to a certain extent through the matrix multiplication shown in (5.3).

$$\boldsymbol{\alpha}' = \mathbf{A}\boldsymbol{\alpha} \tag{5.3}$$

The upper-triangular matrix, $\mathbf{A}$, whose entries, $A_{\gamma\varsigma}$, are populated according to (5.4), maps the Zernike coefficients before the aperture size is changed, $\boldsymbol{\alpha}$, to the Zernike coefficients after the aperture size is changed, $\boldsymbol{\alpha}'$.

$$A_{\gamma\varsigma} = \begin{cases} \dfrac{\sqrt{\varepsilon_\gamma + 1}}{\sqrt{\varepsilon_\varsigma + 1}} (-1)^{\frac{\varepsilon_\gamma - \varepsilon_\varsigma}{2}} \begin{pmatrix} \dfrac{\varepsilon_\gamma + \varepsilon_\varsigma}{2} \\ \dfrac{\varepsilon_\gamma - \varepsilon_\varsigma}{2} \end{pmatrix} \left(\left(\dfrac{R'}{R} \right)^{\varepsilon_\varsigma} - \left(\dfrac{R'}{R} \right)^{\varepsilon_\gamma} \right) \delta\left((-1)^\gamma \tau_\gamma - (-1)^\varsigma \tau_\varsigma \right) & \gamma \le \varsigma \\ 0 & \gamma > \varsigma \end{cases} \tag{5.4}$$

In (5.4), R is the original aperture diameter and R' is the final aperture diameter. Also note that ε and τ have been used to represent the radial degree and azimuthal frequency of Zernike polynomials corresponding to the value of the subscript. Conventionally the radial degree and azimuthal frequency are represented using n and m - however, these variables have already been defined as discrete detector plane coordinates. Table 2 shows the estimated and predicted Zernike coefficients for Nyquist-sampled data.

Table 2: Predicted vs. Estimated Zernikes

	Z4	Z5	Z6	Z7	Z8	Z9	Z10	Z11
Predicted	0.29	0.05	0.00	0.01	0.01	0.01	0.01	0.02
Estimated	0.31	0.06	0.04	0.02	0.17	0.07	0.02	0.47

In Table 3, Zernike coefficients other than Z8 and Z11 are within 1/10th of a wavelength. The differences in Z8 and Z11 could be due to the small but significant presence of higher-order aberrations and failure of the phase retrieval algorithm.

Astigmatism Experiment

An image containing a predictable amount of astigmatism was collected in the past by Zingarelli using the experimental set up shown in Figure 18.

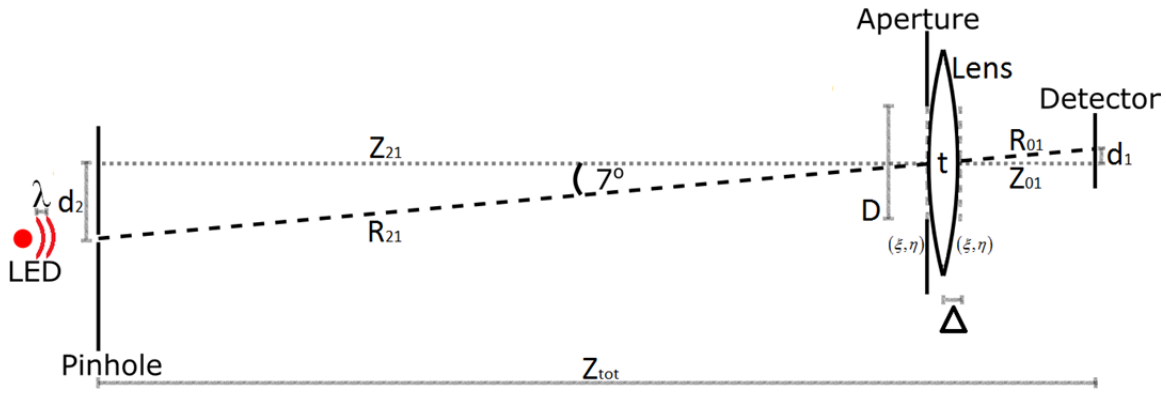

Figure 18: Astigmatism experiment setup.

Table 3: Astigmatism Experiment Setup Measurements

Λ	648 nm	**Z_{tot}**	2.44 m	**D**	10 mm
d_2	22.3 cm	**Z_{21}**	1.74 m	**Λ**	2.2 cm
d_1	-8.5 cm	**Z_{01}**	0.68 m		

A 500 mm focal length lens was used to focus light onto the detector. The position of the pinhole and camera were adjusted laterally to induce astigmatism. Zernike coefficients predicted based on the optical setup of the experiment are shown in . The components of the wave-front, $\phi(\xi,\eta)$, are defined in (5.5)-(5.7), where f_l in (5.7) represents the focal length of the lens.

$$kr_{21}(d_2,0,\xi,\eta) = k\sqrt{(\xi-d_2)^2+\eta^2+z_{21}^2} \tag{5.5}$$

$$kr_{01}(d_1,0,\xi,\eta) = k\sqrt{(\xi+d_1)^2+\eta^2+z_{01}^2} \tag{5.6}$$

$$kt(\xi,\eta) = -\frac{k}{2f_l}\left(\xi^2+\eta^2\right) \tag{5.7}$$

The numerical evaluation of each component of the wave-front (5.5)-(5.7) and are shown in order, from the top left to the bottom right of Figure 19.

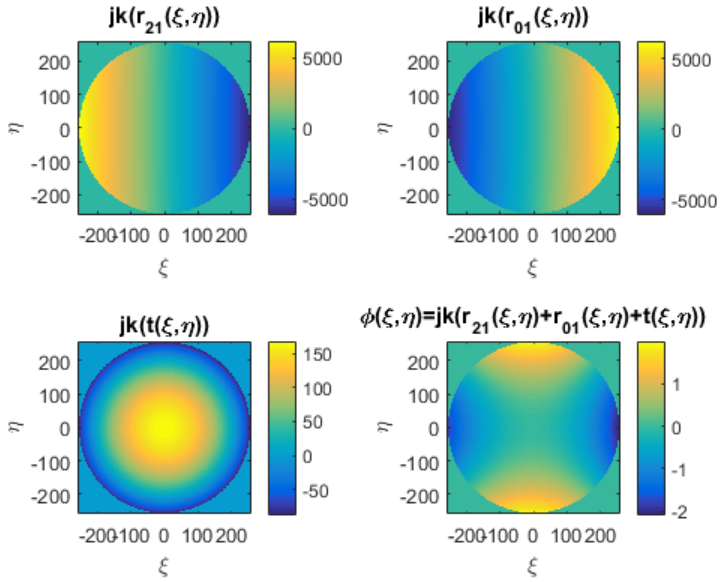

Figure 19: Rayleigh-Sommerfeld Phase.

Predicted Zernike coefficients 2 through 11 are shown in the top row of Table 4 and the corresponding PSF is shown on the left in Figure 22. The absolute error between the decomposed wave-front and the reconstructed wave-front is shown in Figure 20.

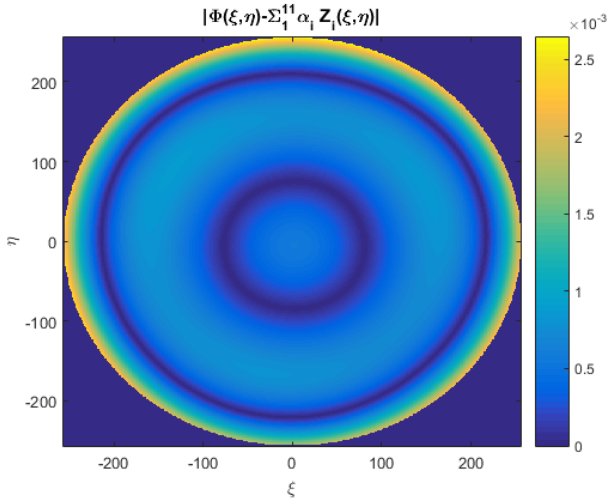

Figure 20: Wavefront residual.

Zernike coefficients 2 through 11 sufficiently characterize the wave-front, as the residual in Figure 20 on the order of 1000^{th} of a wavelength.

Table 4: Zernike Coefficient Magnitudes

	Z4	Z5	Z6	Z7	Z8	Z9	Z10	Z11
Predicted	0.01	0.00	0.77	0.00	0.01	0.00	0.00	0.00
Nyquist	0.07	0.17	0.73	0.05	0.01	0.05	0.04	0.07
Under-sampled	0.03	0.16	0.70	0.04	0.11	0.05	0.07	0.12

The original data obtained from the experiment, shown on the left side in Figure 21, is oversampled by a factor of 1.4. Nyquist-sampled and under-sampled data were not captured. Therefore, the Nyquist-sampled and under-sampled frames shown in the center and the right of Figure 21 were generated in MATLAB.

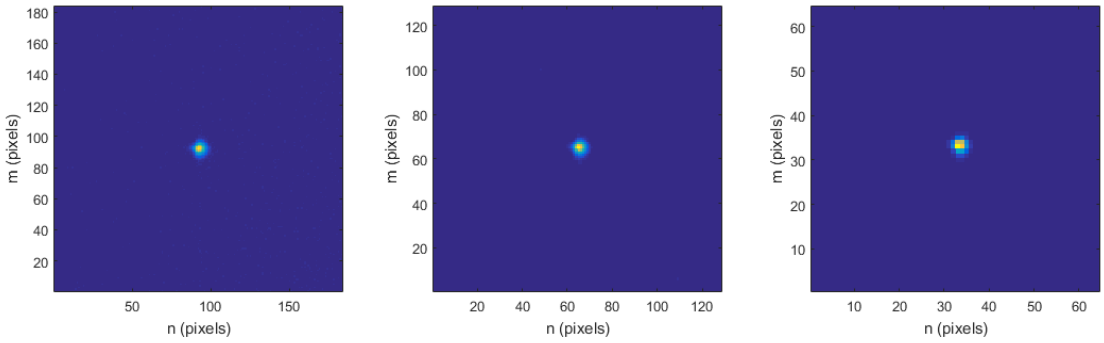

Figure 21: Astigmatism experiment data. Original data (left), generated frames (center, right).

To generate the Nyquist-sampled data, each pixel in the over-sampled frame was split into 7 by 7 pixels. The result was convolved by a 10 by 10 matrix, where each cell has a value of 1/7, and decimated by 10. The under-sampled data was generated by convolving the Nyquist-sampled frame with a 2 by 2 square and decimating by 2. Down-sampling data by a small factor does not cause the data to become unrealistic as long as size of the effective pixel in the down-sampled data is reasonable. The camera used in this

experiment had a pixel pitch of 16µm. The effective pixel pitch in the Nyquist and under-sampled data therefore remain reasonable at 22.4µm and 44.8µm, respectively. Zernike coefficients were retrieved for both Nyquist-sampled and under-sampled cases. The phase retrieval algorithm was performed 100 times with different initial sets of Zernike coefficients 2-11 randomly selected from a normal distribution, and the initial object estimate shown in Figure 13. Of the 100 estimates produced, Zernike coefficients minimizing squared error between the estimated intensity and the data were selected. Final Zernike coefficients estimates from Nyquist and under-sampled data are shown on the second and third row of Table 4. The corresponding PSFs are shown in the center and right of Figure 22.

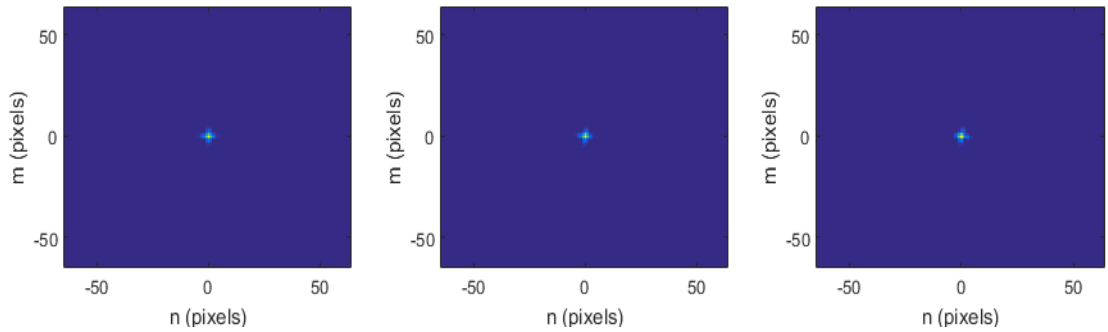

Figure 22: Predicted and estimated PSFs for astigmatism experiment. Predicted PSF (left), PSF from Nyquist data (center), PSF from under-sampled data (right).

Zernike coefficients retrieved from Nyquist-sampled data and from under-sampled data mostly agree. In both cases, the difference between the estimated amount of astigmatism and the predicted amount of astigmatism is under $1/10^{th}$ of a wave.

Atmosphere Experiment

The experimental setup shown in Figure 23 was used to generate 250 frames of data with random atmospheric aberrations. The original data obtained from the experiment was oversampled by a factor of 4. However, in a similar manner to the astigmatism experiment, the data was down-sampled by a factor of 4 to obtain Nyquist data and by a factor of 8 to obtain under-sampled data. Although these down-sampling factors are larger than those used in the astigmatism experiment, the pixel pitch of the camera was also smaller. The resulting effective pixel pitch remains reasonable at 13.8µm for Nyquist-sampled data and 27.6µm for under-sampled data.

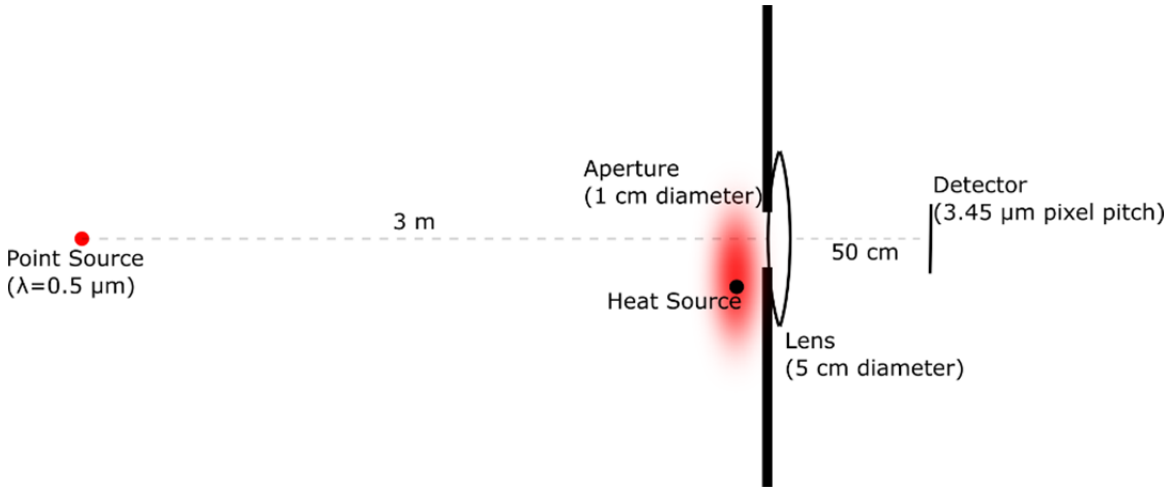

Figure 23: Atmosphere experiment setup.

The mean absolute error between the Zernike coefficients estimated from Nyquist-sampled data and Zernike coefficients estimated from under-sampled data are plotted in Figure 24. Additionally, for 244 out of 250 frames, all Zernike coefficients magnitudes estimated from under-sampled data converged to within half a wave of the estimates from Nyquist-sampled frames.

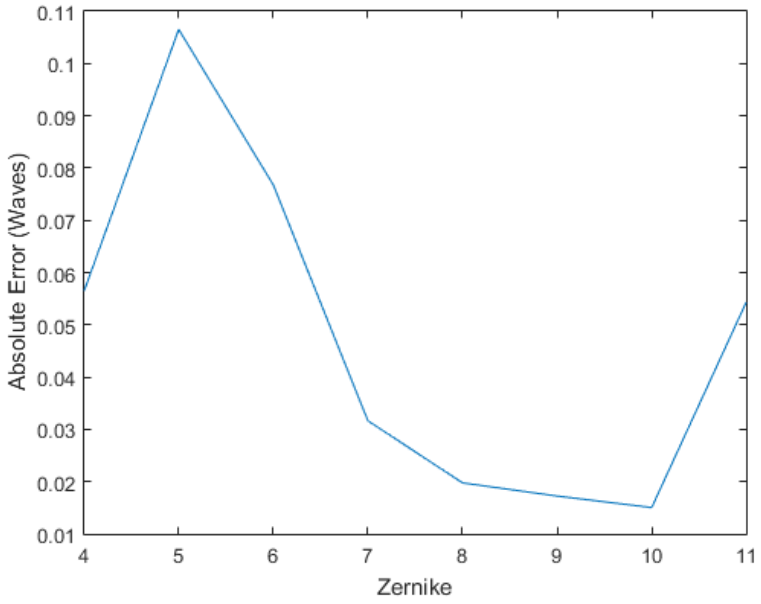

Figure 24: Atmosphere experiment results. Mean absolute error is shown between Zernike coefficient estimates from Nyquist-sampled data and Zernike coefficient estimates from under-sampled data.

VI. Conclusions and Recommendations

Summary

The purpose of this research was to retrieve phase from under-sampled images of astronomical objects. Zernike coefficients 4 through 11 were successfully recovered from noisy, under-sampled data using an algorithm combining blind-deconvolution, GS, and field-based compass. In Chapter 3, update equations for blind deconvolution originally proposed by Schultz were modified for under-sampled data. These update equations were combined with the GS algorithm and the field-based in Chapter 4. Simulation and experiments were conducted in Chapter 5 to evaluate the performance of the newly formed phase retrieval algorithm.

Conclusion

The phase retrieval algorithm often converges to Zernike coefficient estimates with the incorrect sign. However, there was no way of correcting this behavior without additional information. Zernike coefficients with the wrong sign still produced the same PSF as Zernike coefficients with the correct sign. Therefore, Zernike coefficient magnitudes were compared to evaluate the performance of the algorithm.

The algorithm performed well in simulation. The magnitudes of the Zernike coefficient estimates Zernike coefficients converged to within 0.5 waves for 97% of the trials using Nyquist-sampled data and 92% of the trials using under-sampled data. The phase retrieval algorithm worked on real data as well. Zernike coefficients magnitudes converged to predicted values to within $1/10^{th}$ of a wave for Nyquist data and $1/5^{th}$ of a wave for data under-sampled by a factor of 2. Unlike results from the astigmatism data,

estimates from the defocused data could not be compared to a predicted set of coefficients since the optical configuration of the telescope is unknown. Instead, Zernike coefficients recovered from the under-sampled data were compared to those recovered from the Nyquist-sampled data. The magnitude of defocus recovered from Nyquist-sampled data was within 0.02 waves of the value predicted using defocus recovered from data under-sampled by 2. The magnitude of horizontal coma and primary spherical aberration recovered from the Nyquist sampled data differed significantly from values predicted using the under-sampled data, however. Horizontal coma was off by $1/5^{th}$ of a wave while primary spherical aberration was off by half a wave.

Significance

The phase retrieval algorithm developed and evaluated in this thesis is an important step towards a method to analyze and improve the detection capability of optical systems such as star trackers and telescopes, especially since these systems are generally under-sampled. Although under-sampled phase retrieval has been performed in the past the new phase retrieval algorithm is unique because it uses Zernike polynomials to constrain the complexity of the problem, allowing it to quantify the phase using a much smaller set of variables.

Recommendations

A major limitation of this algorithm is that it must be performed multiple times on each frame of data with different initial Zernike coefficient estimates to produce good final estimates. Phase retrieval could be performed significantly faster if the algorithm's

reliance the initial Zernike coefficient estimates were reduced. Alternatively, a method that could quickly determine bad sets of initial Zernike coefficients could be developed.

Additional testing should be performed on the algorithm to determine the extent of its capabilities with worse atmospheric conditions and further under-sampling. For realistic use with telescopes used for space domain awareness such as the GEODSS or the Space Surveillance Telescope, the phase retrieval algorithm will have to work for much larger atmospheric aberrations and under-sampling factors.

Bibliography

[1] S. Kan, "US Department of State," 23 April 2007. [Online]. Available: http://fpc.state.gov/documents/organization/84322.pdf. [Accessed 20 August 2015].

[2] "Orbital Debris Quarterly," April 2009. [Online]. Available: http://orbitaldebris.jsc.nasa.gov/newsletter/pdfs/ODQNv13i2.pdf. [Accessed 20 August 2015].

[3] "National Security Strategy," Feburary 2015. [Online]. Available: https://www.whitehouse.gov/sites/default/files/docs/2015_national_security_strategy.pdf. [Accessed 20 August 2015].

[4] J. R. Feinup, J. C. Marron, T. J. Schultz and J. H. Seldin, "Hubble Space Telescope characterized by using Phase-retrieval algorithms," *Applied Optics,* vol. 32, no. 10, pp. 1747-1767, 1993.

[5] D. F. Woods, R. Shah, J. Johnson, A. Szabo, E. C. Pearce, R. Lambour and W. Faccenda, "The Space Surveillance Telescope: Focus and Alignment of a Three Mirror Telescope," *Optical Engineering,* vol. 52, no. 5, 2013.

[6] A. Tokovinin and S. Heathcote, "Donut: Measuring Optical Aberrations from a Single Extrafocal Image," *Publications of the Astronomical Society of the Pacific,* vol. 118, no. 846, pp. 1165-1175, 2006.

[7] R. W. Gerchberg and W. O. Saxton, "A Practical Algorithm for the Determination of Phase from Image and Diffraction Plane Pictures," *Optik,* vol. 35, no. 2, pp. 237-246, 1972.

[8] K. Itoh, "Analysis of the phase unwrapping algorithm," *Applied Optics,* vol. 21, no. 14, pp. 2470-2470, 1982.

[9] J. C. Zingarelli and S. C. Cain, "Phase Retrieval and Zernike Decomposition Using Measured Intensity Data and Estimated Electric Field," *Applied Optics,* vol. 59, no. 31, pp. 7435-7444, 2013.

[10] J. W. Goodman, Fourier Optics, Englewood: Roberts & Company Publishers, 2005.

[11] J. W. Goodman, Statistical Optics, New York: Wiley, 2000.

[12] T. J. Schultz, "Multiframe Blind Deconvolution of Astronomical Images," *Journal of the Optical Society of America,* vol. 10, no. 5, pp. 1064-1073, 1993.

[13] A. P. Dempster, N. M. Laird and D. B. Rubin, "Maximum Likelihood from Incomplete Data via the EM Algorithm," *Journal of the Royal Statistical Society,* vol. 39, no. 1, pp. 1-38, 1977.

[14] G. Casella and R. L. Berger, Statistical Inference, Pacific Grove: Duxbury, 2002.

[15] B. J. Neff, Q. D. Macmanus, S. C. Cain and R. K. Martin, "Image deblurring and near-real-time atmospheric seeing estimation through the employment of convergence of variance," *Journal of Applied Remote Sensing,* vol. 7, no. 1, 2013.

[16] T. G. Kolda, R. M. Lewis and V. Torczon, "Optimization by Direct Search: New Perspectives on Some Classical and Modern Methods," *SIAM Review,* vol. 45, no. 3, pp. 385-482, 2003.

REPORT DOCUMENTATION PAGE

Form Approved
OMB No. 074-0188

1. REPORT DATE *(DD-MM-YYYY)*	**2. REPORT TYPE**	**3. DATES COVERED** *(From – To)*
24-03-2016	Master's Thesis	Sept. 2014 – March 2016

TITLE AND SUBTITLE

Field-based phase retrieval using under-sampled data

5a. CONTRACT NUMBER

5b. GRANT NUMBER

5c. PROGRAM ELEMENT NUMBER

6. AUTHOR(S)

Watts, Tatsuki, L., 2nd Lt., USAF

5d. PROJECT NUMBER

5e. TASK NUMBER

5f. WORK UNIT NUMBER

7. PERFORMING ORGANIZATION NAMES(S) AND ADDRESS(S)
Air Force Institute of Technology
Graduate School of Engineering and Management (AFIT/EN)
2950 Hobson Way
WPAFB OH 45433-7765

8. PERFORMING ORGANIZATION REPORT NUMBER

AFIT-ENG-MS-16-M-051

9. SPONSORING/MONITORING AGENCY NAME(S) AND ADDRESS(ES)
AGENCY intentionally left blank
ADDRESS
PHONE and EMAIL
ATTN: POC

10. SPONSOR/MONITOR'S ACRONYM(S)

11. SPONSOR/MONITOR'S REPORT NUMBER(S)

12. DISTRIBUTION/AVAILABILITY STATEMENT
DISTRUBTION STATEMENT A. APPROVED FOR PUBLIC RELEASE; DISTRIBUTION UNLIMITED.

13. SUPPLEMENTARY NOTES
This material is declared a work of the U.S. Government and is not subject to copyright protection in the United States.

14. ABSTRACT
A phase retrieval algorithm designed for use with under-sampled astronomical data is developed in this thesis. Blind-deconvolution, Gerchberg Saxton (GS), and a field-based compass search are combined into an algorithm capable of recovering Zernike coefficients 4 through 11 from single frames of noisy, under-sampled data without the need to unwrap the recovered phase. The performance of the algorithm in data under-sampled by a factor of 2 is compared the performance of the algorithm on Nyquist-sampled data.

In simulation trials, the magnitudes of all 8 estimated Zernike coefficients converged to within half a wave of the true values for 98% of the Nyquist-sampled frames and 92% under-sampled frames. The simulation was conducted using 100 frames of point-source data generated by randomly choosing Zernike coefficients 2 through 11 from a normal distribution. Phase retrieval was performed on defocused data and data containing an astigmatism aberration. For the astigmatism data, the estimated Zernike coefficient magnitudes were within 1/10th of a wave for Nyquist data and 1/5th of a wave for data under-sampled by a factor of 2. The magnitude of defocus recovered from Nyquist-sampled data was within 0.02 waves of the value predicted using defocus recovered from data under-sampled by 2.

15. SUBJECT TERMS
Optical Imaging, Space Domain Awareness, Point Spread Function, Aberration, Phase Retrieval, Blind Deconvolution, Gerchberg-Saxton, Zernike Polynomials

16. SECURITY CLASSIFICATION OF:			**17. LIMITATION OF ABSTRACT**	**18. NUMBER OF PAGES**	**19a. NAME OF RESPONSIBLE PERSON**, Stephen C. Cain, AFIT/ENG
a. REPORT	**b. ABSTRACT**	**c. THIS PAGE**			**19b. TELEPHONE NUMBER** *(Include area code)*
U	**U**	**U**	**UU**	76	(937) 255-6565, ext 4716 (Stephen.cain@afit.edu)

Standard Form 298 (Rev. 8-98)
Prescribed by ANSI Std. Z39-18